New Observations of Upper Tropospheric NO₂ from TROPOMI

Eloise A. Marais[1,2], John F. Roberts[3], Robert G. Ryan[4,5], Henk Eskes[6], K. Folkert Boersma[6,7], Sungyeon Choi[8,9], Joanna Joiner[8], Nader Abuhassan[8,10], Alberto Redondas[11], Michel Grutter[12], Alexander Cede[13], Laura Gomez[14,15], Monica Navarro-Comas[14]

5 [1]Department of Geography, University College London, London, UK
[2]School of Physics and Astronomy, University of Leicester, Leicester, UK
[3]Centre for Landscape and Climate Research, University of Leicester, Leicester, UK
[4]School of Earth Sciences, The University of Melbourne, Melbourne, Australia
[5]ARC Centre of Excellence for Climate System Science, Sydney, Australia
10 [6]Satellite Observations Department, Royal Netherlands Meteorological Institute (KNMI), De Bilt, the Netherlands
[7]Meteorology and Air Quality Group, Wageningen University (WUR), Wageningen, the Netherlands
[8]NASA Goddard Space Flight Center, Greenbelt, MD, USA
[9]Science Systems and Applications, Inc., Lanham, MD, USA
[10]Joint Center for Earth Systems Technology, University of Maryland, Baltimore County, Baltimore, MD, USA
15 [11]Izaña Atmospheric Research Center, AEMET, Tenerife, Canary Islands, Spain
[12]Centro de Ciencias de la Atmósfera, Universidad Nacional Autónoma de México, Mexico City, Mexico
[13]LuftBlick, Fritz-Konzert-Straße 4, Innsbruck, Austria
[14]Instituto Nacional de Técnica Aeroespacial (INTA), Área de Investigación e Instrumentación Atmosférica, Ctra Ajalvir km4, 28850, Torrejón de Ardoz, Madrid, Spain
20 [15]Groupe de Spectrométrie Moléculaire et Atmosphérique, URM CNRS 7331, UFR Sciences Exactes et Naturelles, Moulin de la Housse, BP 1039, 51687 Reims CEDEX 2, France

Correspondence to: Eloise A. Marais (e.marais@ucl.ac.uk)

Abstract. Nitrogen oxides ($NO_x \equiv NO + NO_2$) in the NO_x-limited upper troposphere (UT) are long-lived and so have a large influence on the oxidizing capacity of the troposphere and formation of the greenhouse gas ozone. Models misrepresent NO_x

25 in the UT and observations to address deficiencies in models are sparse. Here we obtain a year of near-global seasonal mean mixing ratios of NO_2 in the UT (450-180 hPa) at $1° \times 1°$ by applying cloud-slicing to partial columns of NO_2 from TROPOMI. This follows refinement of the cloud-slicing algorithm with synthetic partial columns from the GEOS-Chem chemical transport model. We find that synthetic cloud-sliced UT NO_2 are spatially consistent (R = 0.64) with UT NO_2 calculated across the same cloud pressure range and scenes as are cloud-sliced ("true" UT NO_2), but the cloud-sliced UT NO_2 is 11-22% more than the

30 "true" all-sky seasonal mean. The largest contributors to differences between synthetic cloud-sliced and "true" UT NO_2 are target resolution of the cloud-sliced product and uniformity of overlying stratospheric NO_2. TROPOMI, prior to cloud-slicing, is corrected for a 13% underestimate in stratospheric NO_2 variance and a 50% overestimate in free tropospheric NO_2 determined by comparison to Pandora total columns at high-altitude sites in Mauna Loa, Izaña and Altzomoni, and MAX-DOAS and Pandora tropospheric columns at Izaña. Two cloud-sliced seasonal mean UT NO_2 products for June 2019 to May

35 2020 are retrieved from corrected TROPOMI total columns using distinct TROPOMI cloud products that assume clouds are reflective boundaries (FRESCO-S) or water droplet layers (ROCINN-CAL). TROPOMI UT NO_2 typically ranges from 20-30 pptv over remote oceans to >80 pptv over locations with intense seasonal lightning. Spatial coverage is mostly in the tropics

and subtropics with FRESCO-S and extends to the midlatitudes and polar regions with ROCINN-CAL, due to its greater abundance of optically thick clouds and wider cloud top altitude range. TROPOMI UT NO_2 seasonal means are spatially consistent (R = 0.6-0.8) with an existing coarser spatial resolution (5° latitude × 8° longitude) UT NO_2 product from the Ozone Monitoring Instrument (OMI). UT NO_2 from TROPOMI is 12-26 pptv more than that from OMI due to increase in NO_2 with altitude from the OMI pressure ceiling (280 hPa) to that for TROPOMI (180 hPa), but possibly also systematic altitude differences between the TROPOMI and OMI cloud products. The TROPOMI UT NO_2 product offers potential to evaluate and improve representation of UT NO_x in models and supplement aircraft observations that are sporadic and susceptible to large biases in the UT.

1 Introduction

Nitrogen oxides ($NO_x \equiv NO+NO_2$) in the upper troposphere (UT; ~8-12 km) influence the oxidizing capacity of the atmosphere and global climate, as the formation and radiative forcing of tropospheric ozone are most efficient in the NO_x-limited UT (Mickley et al., 1999; Bradshaw et al., 2000; Dahlmann et al., 2011; Worden et al., 2011). Sources of NO_x to the UT include local emissions from lightning and cruising altitude aircraft, deep convective uplift of surface pollution, downwelling from the stratosphere, long-range transport, and chemical recycling of NO_x from stable reservoir compounds (Ehhalt et al., 1992; Lamarque et al., 1996; Schumann, 1997; Jaeglé et al., 1998; Bradshaw et al., 2000; Bertram et al., 2007). The lifetime of NO_x in the UT varies from a few hours to a few days depending on availability of hydrogen oxides ($HO_x \equiv OH + HO_2$) and peroxy radicals (RO_2) to convert NO_x to reservoir compounds (Jaeglé et al., 1998; Bradshaw et al., 2000; Nault et al., 2016).

Current understanding of UT NO_x is erroneous, as demonstrated by misrepresentation in chemical transport models (CTMs) of the vertical distribution, relative abundance (ratios of NO-to-NO_2), and absolute magnitude of UT NO_x when compared to in situ measurements from research aircraft (Boersma et al., 2011; Travis et al., 2016; Silvern et al., 2018). Models are used to determine the contribution of ozone to anthropogenic climate change in the absence of reliable historical measurements (Pavelin et al., 1999). Models also provide prior information about the vertical distribution of NO_2 for retrieval of vertical column densities of NO_2 from space-based UV-visible instruments. Errors in these retrievals are particularly vulnerable to biases in modelled UT NO_2, due to greater sensitivity of space-based observations to the UT than the middle and lower troposphere (Travis et al., 2016; Silvern et al., 2019). This impedes accurate top-down inference of air quality variability, surface concentrations and precursor emissions (Stavrakou et al., 2013; Silvern et al., 2019). Models include heavily parameterized representation of lighting (Tost et al., 2007; Allen et al., 2010; Ott et al., 2010; Murray et al., 2012; Murray et al., 2013), the largest global influencer of NO_x in the UT (Bradshaw et al., 2000; Marais et al., 2018), and may misrepresent the reaction kinetics and physical processing of NO_x for the cold, low-pressure conditions of the UT (Chang et al., 2011; Henderson et al., 2011; 2012; Stavrakou et al., 2013; Amedro et al., 2019).

70   Observations that have been used to better understand UT NO$_x$ are mostly limited to research and commercial aircraft campaigns. For research aircraft, the record of observations in the UT since the early 1990s have been sustained almost exclusively by the NASA DC8 plane, with recent contributions from the German High Altitude and Long Range Research Aircraft (HALO) (Wendisch et al., 2016). There are also commercial aircraft campaigns, but these are prevalent over heavily trafficked flight corridors and are often in the stratosphere at cruising altitude (Thomas et al., 2015; Stratmann et al., 2016). In

75   situ measurements of NO$_2$ in the UT can also be biased by interference from NO$_x$ reservoir compounds that thermally decompose to NO$_2$ in the instrument inlet (Browne et al., 2011; Reed et al., 2016). Standard remote sensing products of NO$_2$ from space-based nadir- and limb-viewing instruments provide global coverage, but either as a single piece of vertical information in the troposphere in the nadir as tropospheric column densities (Levelt et al., 2018) or as vertically resolved NO$_2$ in the limb limited to NO$_2$ abundances above the tropopause (Newchurch et al., 1996; Sioris et al., 2004; Brohede et al., 2007;

80   Jones et al., 2012).

Near-global research products of seasonal mean vertically resolved tropospheric NO$_2$ have been retrieved by applying the cloud-slicing technique to partial columns of NO$_2$ from the space-based Ozone Monitoring Instrument (OMI) (Choi et al., 2014; Belmonte-Rivas et al., 2015). Cloud-slicing involves regressing clusters of partial NO$_2$ columns above optically thick

85   clouds against corresponding cloud top pressures. The resultant regression slopes are converted to NO$_2$ mixing ratios that represent average NO$_2$ across the cloud top altitude range (Ziemke et al., 2001). The advantages of cloud-slicing include enhanced signal over bright optically thick clouds (van der A et al., 2020) and removal of the dry stratosphere due to lack of clouds there. Near-global multiyear (2005-2007) seasonal means of UT NO$_2$ from cloud-sliced OMI partial columns have been shown to reproduce the spatial variability of UT NO$_2$ measured with bias-corrected NASA DC8 aircraft measurements of NO$_2$

90   over North America, though at very coarse scales (seasonal, 32° × 20°) (Marais et al., 2018). Even so, the OMI product confirms the dominant global influence of lightning on UT NO$_x$ and provides global constraints on lightning NO$_x$ production rates (280 ± 80 moles NO$_x$ per lightning flash) and annual lightning NO$_x$ emissions (5.9 ± 1.7 Tg N) (Marais et al., 2018). OMI pixels are at relatively coarse resolution (13 km × 24 km at nadir) and there is substantial data loss after 2007 due to the so-called row anomaly (Schenkeveld et al., 2017; Torres et al., 2018). The recently launched (October 2017) TROPOMI

95   instrument on the Sentinel-5P satellite has the same spatial coverage as pre-row-anomaly OMI (swath width of 2600 km), but with a finer nadir pixel resolution of 7.2 km × 3.5 km (along track × across track) until 5 August 2019, further refined thereafter to 5.6 km × 3.5 km (Argyrouli et al., 2019). This offers better cloud-resolving capability and greater data pixel density than OMI with potential to retrieve finer resolution NO$_2$ in the UT.

100   Here we refine and test the cloud-slicing retrieval using synthetic partial NO$_2$ columns from the GEOS-Chem CTM before retrieving UT NO$_2$ from TROPOMI partial NO$_2$ columns with cloud information from two distinct TROPOMI cloud products. Application of cloud-slicing to TROPOMI follows evaluation of TROPOMI total, stratospheric and tropospheric columns with

ground-based measurements of NO$_2$ from Pandora and Multi-axis differential optical absorption spectroscopy (MAX-DOAS) at free tropospheric monitoring sites. We also evaluate TROPOMI UT NO$_2$ with the OMI UT NO$_2$ product.

2 Cloud-slicing of GEOS-Chem synthetic partial columns

Targeting cloudy scenes could yield representation errors in NO$_2$ mixing ratios in the UT, due to the influence of clouds on NO$_x$ photochemistry (Holmes et al., 2019), large enhancements in NO$_x$ from lightning and convective uplift of surface pollution that accompany cloud formation (Price and Rind, 1992; Bertram et al., 2007), and low sampling frequency due to strict data filtering (Choi et al., 2014). We test the ability of the cloud-slicing technique to return accurate, representative mixing ratios of NO$_2$ in the UT by applying this technique to synthetic partial columns from GEOS-Chem. The "true" NO$_2$ used to evaluate cloud-sliced NO$_2$ is obtained by averaging NO$_2$ across the same vertical range as the cloud-sliced NO$_2$ for the same cloudy model grid squares as are cloud-sliced ("true" cloudy UT NO$_2$) and for all clear and cloudy model grid squares ("true" all-sky UT NO$_2$).

Synthetic NO$_2$ are from GEOS-Chem version 12.1.0 (https://doi.org/10.5281/zenodo.1553349; last accessed 10 August 2019) simulated at a horizontal resolution of 0.25° × 0.3125° (latitude × longitude) extending over 47 vertical layers from the surface to 0.01 hPa for the nested domains available in version 12.1.0. These include North America (9.75-60°N, 130-60°W), western Europe (30-70°N, 15°W-61.25°E), and Southeast Asia (15-55°N, 70-140°E). Dynamic (3-hourly) boundary conditions are from a coarse resolution (4° × 5°) global GEOS-Chem simulation. The model is driven with NASA GEOS-FP assimilated meteorology and includes comprehensive emission inventories from anthropogenic and natural sources. These include local emissions of NO$_x$ in the UT from lightning as described by Murray et al. (2012) and from aircraft using the Aviation Emissions Inventory Code (AEIC) inventory detailed in Stettler et al. (2011). The model is simulated in boreal summer (June-August) when variability in UT NO$_x$ in all nested domains is dominated by lightning (Marais et al., 2018). The model is sampled daily at 12h00-15h00 local time (LT) to be consistent with the TROPOMI overpass time (13h30 LT). Two years (2016 and 2017) are simulated to increase data density. The model years predate TROPOMI, but this has no bearing on assessment of the cloud-slicing technique.

The cloud-slicing approach we apply to synthetic partial columns above synthetic clouds to estimate seasonal means of UT NO$_2$ is the same as will be applied to TROPOMI, so model variables are only used if these are also available in or can be derived from publicly available TROPOMI data products. GEOS-Chem daily partial NO$_2$ column densities (stratosphere + partial troposphere) and the corresponding GEOS-FP cloud top pressures at 450-180 hPa and 0.25° × 0.3125° are gathered into grid squares of the target resolution of 4° × 5°. These are then screened to remove clusters with non-uniform GEOS-Chem stratospheric NO$_2$ (stratospheric column NO$_2$ relative standard deviation > 0.02) using GEOS-FP thermal tropopause heights to determine the vertical extent of the stratosphere in the model. For a target resolution of 4° × 5° clusters of as many as 256
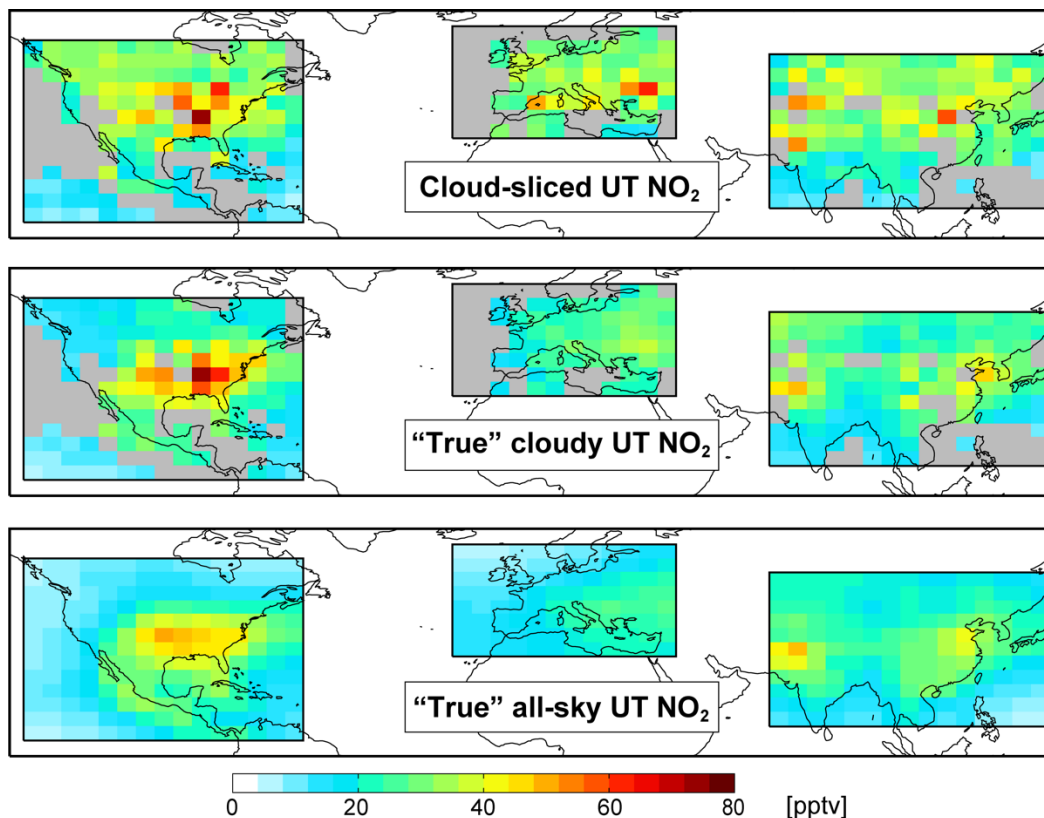
135    $0.25° \times 0.3125°$ partial columns are likely, so we increase the number of possible cloud-sliced NO_2 retrievals by subdividing clusters of at least 100 partial NO_2 columns into scenes of at least 40. This doubles the number of cloud-sliced NO_2 data used to obtain multiyear seasonal means. Additional filtering is applied to clusters to remove extreme NO_2 partial columns (partial columns falling outside the 10th to 90th percentile range) that have a large influence on regression of NO_2 partial columns against cloud top pressures, clusters with fewer than 10 partial columns after screening for extreme values, and clusters that

140   do not extend across a sufficiently wide altitude range (cloud top pressure range ≤ 140 hPa and standard deviation ≤ 30 hPa). GEOS-Chem cloud top heights are diagnosed in the model as the pressure at the top edge of the highest model layer of GEOS-FP upward moist convective mass flux.

The slope of the relationship between cloud top heights and partial columns for each cluster is estimated with reduced major

145   axis (RMA) regression and the error on the slope with bootstrap resampling. Additional filtering is applied to retain slopes that have low relative error (relative error on the slope ≤ 1.0). Large local enhancements in NO_2 at high altitudes that lead to negative slopes and negative cloud-sliced UT NO_2 are diagnosed as slopes significantly less than zero (sum of slope and slope error < 0) and removed. The retained slopes and errors (in molecules cm^{-2} hPa^{-1}) are converted to mixing ratios (in pptv) and outliers caused by steep slopes (UT $NO_2 > 200$ pptv) removed. A threshold of 200 pptv is used, as this far exceeds the maximum

150   seasonal mean UT NO_2 of 145 pptv in the OMI cloud-sliced UT NO_2 product (Marais et al., 2018). We find though that only 3 cloud-sliced retrievals exceed 200 pptv. Seasonal means are obtained by Gaussian weighting individual estimates of cloud-sliced UT NO_2 to the pressure centre (315 hPa).

The cloud-slicing retrieval adopted here is mostly similar to that applied to OMI to estimate mid-tropospheric NO_2 at 900-650

155   hPa (Choi et al., 2014) and UT NO_2 at 450-280 hPa (Marais et al., 2018). We extend the ceiling of the retrieval to 180 hPa (~12.5 km) to better capture the vertical extent of the upper troposphere. Another notable distinction is that the method applied to OMI used vertical gradients of NO_2 from the NASA Global Modeling Initiative (GMI) CTM to diagnose scenes with non-uniform NO_2 using a threshold of 0.33 pptv hPa^{-1}. We dispense with this step, as its application to TROPOMI requires a model at a similar fine spatial resolution to TROPOMI and CTMs may underestimate vertical NO_2 gradients in the UT (Boersma et

160   al., 2011; Travis et al., 2016; Silvern et al., 2018). Anyway, we find that the strict filtering applied to GEOS-Chem partial columns removes most (88%) scenes with NO_2 vertical gradients ≥ 0.33 pptv hPa^{-1}.

Figure 1 shows GEOS-Chem seasonal mean cloud-sliced and "true" cloudy UT NO_2 at $4° \times 5°$. The latter is also Gaussian weighted to 315 hPa. The uncertainty in individual cloud-sliced values, estimated as the RMA regression slope error, range

165   from 6% to the imposed error limit, 99%. This is reduced to <2% for the multiyear seasonal means in Figure 1 due to temporal averaging. Agreement between the cloud-sliced and "true" cloudy UT NO_2 is shown in the scatterplot in Figure 2. Successful cloud-sliced retrievals can exceed 35 for many grid squares, though these do not exhibit better agreement with the "truth" than
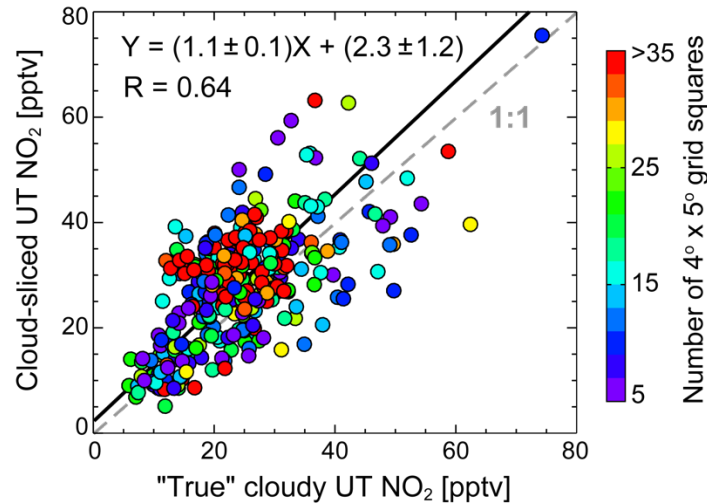
the grid squares with fewer (<10) retrievals. The two datasets are spatially consistent (R = 0.64) and exhibit similar variance (slope = 1.1 ± 0.1). The cloud-sliced UT NO_2 has a small positive offset in background UT NO_2 (intercept = 2.3 ± 1.2 pptv).

170   On average, cloud-sliced UT NO_2 is 17% more than the "true" cloudy UT NO_2, but this depends on the spatial resolution of the retrieved cloud-sliced product. Regression slopes increase from 0.87 ± 0.03 for cloud-sliced UT NO_2 obtained at 2° × 2.5° to 1.4 ± 0.2 at 8° × 10° and the cloud-sliced UT NO_2 is 4.1% less than the "true" cloudy UT NO_2 at 2° × 2.5° and 37% more at 8° × 10°. Maps of synthetic cloud-sliced UT NO_2 at 2° × 2.5° and 8° × 10° are in Figure S1. Strict data filtering in the cloud-slicing steps removes 90% of the clusters of GEOS-Chem partial columns for the 4° × 5° product. Most (33%) data loss is due

175   to the strict relative standard deviation threshold applied to stratospheric NO_2. Cloud-slicing is very sensitive to this threshold. Relaxing it from a relative standard deviation of 0.02 to 0.03 increases data retention from 10% of the clusters of GEOS-Chem partial columns to 17%, but increases the positive bias in cloud-sliced UT NO_2 from 17% to 45%, This is due to an increase in the contribution of variability in the stratosphere to the cloud-slicing regression slopes.

180

Figure 1: Comparison of synthetic cloud-sliced and "true" NO_2 in the upper troposphere (UT) for June-August 2016-2017. Maps show UT NO_2 at 4° × 5° from cloud-slicing GEOS-Chem partial columns above all clouds with cloud top pressures at 450-180 hPa (top), as grid-average mixing ratios from GEOS-Chem for the same scenes as are cloud-sliced (middle) and for all-sky (clear and cloudy) scenes (bottom). Data are Gaussian weighted to the pressure centre (315 hPa). Grey grids have <5 data points.

6

185 Also shown in Figure 1 is the "true" all-sky UT NO_2 obtained for all (cloudy and clear) scenes across 450-180 hPa. Model grids with stratospheric influence are identified and removed using GEOS-FP tropopause heights that are updated hourly in the model. The "true" cloudy UT NO_2 is 17% more than all-sky UT NO_2. Spatial resolution influences the size of this difference, increasing from 11% at $2° \times 2.5°$ to 22% at $8° \times 10°$. This suggests that isolating cloudy scenes induces a 11-22% bias in seasonal mean NO_2 that could be due to a combination of poor data retention (low sampling frequency of cloudy

190 scenes), the influence of clouds on NO_x photochemistry (Pour-Biazar et al., 2007; Holmes et al., 2019), and local enhancements in NO_x from events like lightning and deep convective uplift of surface pollution that accompany clouds (Crawford et al., 2000; Ridley et al., 2004; Bertram et al., 2007).

195 **Figure 2: Scatter plot of synthetic cloud-sliced versus "true" cloudy NO_2 in the upper troposphere (UT). Points are $4° \times 5°$ seasonal means from Figure 1 (top and middle panels) coloured by the number of successful cloud-sliced retrievals. Values inset are the RMA regression statistics and Pearson's correlation coefficient (R). Slope and intercept errors are from bootstrap resampling.**

Cloud-slicing applied to GEOS-Chem considers all cloudy scenes, whereas cloud-slicing of satellite observations is applied to partial columns above optically thick clouds to minimise contamination of NO_2 from below the cloud. If we only consider

200 synthetic partial columns above clouds with a physical (geometric) cloud fraction across 450-180 hPa of at least 0.7, the cloud-sliced UT NO_2 positive difference is similar (18%) to that obtained for all cloudy scenes, but half the amount of data is retained. The cloud fraction retrieved from TROPOMI is an effective or radiometric cloud fraction that is systematically less than the physical cloud fraction from the model. Our results suggest that representation error is not sensitive to the cloud fraction threshold. Another distinction in GEOS-Chem and TROPOMI cloud variables is that the model provides the physical cloud

205 top height, whereas TROPOMI cloud retrievals that use models that assume clouds are uniform reflective boundaries retrieve cloud top heights that can be ~1 km lower than the physical cloud top (Joiner et al., 2012; Choi et al., 2014; Loyola et al., 2018a). We again apply the cloud-slicing algorithm to the simulated partial columns, but with the cloud top heights artificially reduced by 1 km. This approach assumes that the difference in altitudes of effective (radiometric) clouds and physical clouds

is systematic and vertically and horizontally uniform. The difference between the resultant cloud-sliced UT NO_2 and the "true" cloudy UT NO_2 shown in the middle panel of Figure 1 increases from 17% to 24%. This is because the decrease in cloud top altitude leads to a larger increase in the vertical extent of partial columns above high-altitude clouds than those above low-altitude clouds leading to steeper regression slopes and larger UT NO_2.

3 Evaluation of TROPOMI with ground-based instruments at high-altitude sites

Pandora spectrometer systems provide observations of total and tropospheric columns of NO_2 using direct sun, direct moon and sky radiance observations (Herman et al., 2009; Cede et al., 2019). Those at high-altitude sites have limited influence from the planetary boundary layer and so are used here to evaluate free tropospheric and stratospheric NO_2 from TROPOMI. These include long-term Pandora instruments at Mauna Loa, Hawaii (19.48°N, 155.60°W, 4.2 km above sea level or a.s.l, ~600 hPa), Izaña, Tenerife, Canary Islands (28.31°N, 16.50°W, 2.4 km a.s.l, ~760 hPa), and Altzomoni, Mexico (19.12°N, 98.66°W, 4.0 km a.s.l, ~620 hPa). Mauna Loa and Izaña are remote and have limited anthropogenic influence (Toledano et al., 2018), whereas Altzomoni is ~70 km southeast of Mexico City and is often within the mixed layer of the city in the afternoon (Baumgardner et al., 2009) after the TROPOMI overpass. On average, multiyear mean tropospheric NO_2 columns from OMI are ~10×10^{15} molecules cm^{-2} lower over Altzomoni (<5×10^{15} molecules cm^{-2}) than the city (>15×10^{15} molecules cm^{-2}) (Rivera et al., 2013). At Izaña, there is also a MAX-DOAS instrument that we use to retrieve tropospheric columns of NO_2 to assess Pandora and TROPOMI. MAX-DOAS offers vertical sensitivity in the troposphere and has been used extensively to determine free tropospheric concentrations of NO_2 at high-altitude sites (Gomez et al., 2014; Gil-Ojeda et al., 2015; Schreier et al., 2016).

Pandora level 2 total and tropospheric columns are from the Pandonia Global Network (PGN) (http://data.pandonia-global-network.org/; last accessed 1 June 2020). We use version 1.7 "nvh1" retrieval of total columns and "nvs1" retrieval of tropospheric columns (described below). Observations are for a full year (1 June 2019 to 31 May 2020) at Izaña. The data record is shorter at Mauna Loa (ends 29 March 2020) and Altzomoni (ends 9 March 2020). Total slant columns (NO_2 abundances along the instrument viewing path) are retrieved by fitting a fourth order polynomial to spectra at 400-440 nm using an NO_2 effective temperature of 254.4 K. These are then converted to total vertical column densities by accounting for the geometry of the viewing path (Cede et al., 2019). The Pandora tropospheric NO_2 columns have not yet been validated against other observations. Retrieval of these involves simultaneous retrieval of slant columns of NO_2 and the O_2-O_2 dimer at multiple elevation angles (typically 0°, 60°, 75°, 88°, and 89°). The O_2-O_2 dimer slant columns are used to calculate a representative air mass factor (AMF) that is applied to the difference in NO_2 slant columns at multiple pointing elevation angles to calculate a tropospheric vertical column. The data also include estimates of the uncertainty on the total and tropospheric columns due to instrument noise and atmospheric variability (Cede et al., 2019). The NO_2 effective temperature used in the total NO_2 column retrieval is greater than the column average ambient temperature at high-altitude sites. This

induces a positive bias in the total columns estimated by Verhoelst et al. (2020) to be ~10% that we address by downscaling the Pandora total columns and associated errors by 10%. No correction is applied to the tropospheric columns, due to variable contribution of the troposphere to the total column.

245 MAX-DOAS vertical tropospheric columns of NO_2 at Izaña are from RASAS-II sky radiance spectra for June 2019 to February 2020. The spectra are fitted for NO_2 and O_2-O_2 in the wavelength range 425-490 nm and slant columns are calculated as the difference between these spectra at high-sun (90° instrument elevation angle) and multiple elevation angles (1°, 2°, 3°, 5°, 10°, 30°, and 70°) (Hönninger et al., 2004; Gil et al., 2008; Puentedura et al., 2012; Gomez et al., 2014; Gil-Ojeda et al., 2015). Vertical columns are estimated using optimal estimation that solves an ill-constrained problem by introducing prior

250 information (Rogers, 2000). Prior information for Izaña includes fixed (with altitude) aerosol extinction of 0.01 km^{-1} and NO_2 of 20 pptv from the surface to the tropopause. Aerosol abundances at Izaña are sometimes influenced by windblown dust from the Sahara Desert, but are typically low (aerosol optical depth or AOD < 0.05) (Gomez et al., 2014; Gil-Ojeda et al., 2015). The prior NO_2 profile is within the range of background NO_2 in the UT (10-20 pptv) (Marais et al., 2018) and MAX-DOAS NO_2 concentrations previously retrieved at Izaña (20-40 pptv) (Gomez et al., 2014). Filtering is applied to remove vertical

255 column retrievals with limited independent information (degrees of freedom for signal < 1), and significant light path attenuation by aerosols (AOD > 0.1) and clouds (effective cloud fraction > 0.5). AOD is derived with MAX-DOAS O_2-O_2 dimer differential slant columns retrieved over the same wavelength range as NO_2 (Frieß et al., 2006) and cloud fraction is from the Fast Retrieval Scheme for Clouds from the Oxygen A band version S (FRESCO-S) product provided with the TROPOMI NO_2 product. Filtering removes 40% of the retrieved vertical tropospheric NO_2 columns at Izaña.

260

TROPOMI data is from the Sentinel-5P Pre-Operations Data Hub (https://s5phub.copernicus.eu/dhus/; last accessed 15 June 2020). We use a year of NO_2 data (1 June 2019 to 31 May 2020) from the level 2 offline (OFFL) product version 01-03-02. The data product includes NO_2 abundances along the optical path from the sun to the instrument (the total slant column or SCD_{tot}), NO_2 vertical column densities in the stratosphere (VCD_{strat}), and the stratospheric air mass factor (AMF_{strat}). A detailed

265 description of retrieval of SCD_{tot} and VCD_{strat} is described in the product Algorithm Theoretical Basis Document (van Geffen et al., 2019) and by van Geffen et al. (2020). In brief, SCD_{tot} are obtained by spectral fitting of TROPOMI top-of-atmosphere radiances at 405-465 nm by accounting for light absorption by NO_2 and other relevant gases. VCD_{strat} are from assimilation of TROPOMI and modelled total slant columns over locations diagnosed by the model to have limited tropospheric influence (predominantly remote oceans) (Boersma et al., 2004; Dirksen et al., 2011; van Geffen et al., 2019). The modelled slant

270 columns are the product of vertical columns from the TM5-MP CTM (Williams et al., 2017) and AMFs calculated using TROPOMI viewing geometries and surface reflectivities. The CTM is simulated at 1° × 1° and driven with ECMWF meteorology updated every 3 hours. SCD_{tot} are separated into a stratospheric (SCD_{strat}) and tropospheric (SCD_{trop}) component and a tropospheric AMF (AMF_{trop}) is applied to SCD_{trop} to obtain tropospheric vertical columns (VCD_{trop}). AMF_{trop} accounts for viewing geometry, surface reflectivity, atmospheric absorption and scattering of light by trace gases and aerosols, and

sensitivity to the vertical distribution of NO$_2$. A vertically resolved correction is also applied to the AMF$_{trop}$ to correct for the fixed NO$_2$ effective temperature (220 K) used to retrieve SCD$_{tot}$. The light path in the UT is relatively unobstructed by aerosols and, for cloud-slicing, would mostly be impacted by treatment of the reflectivity of optically thick clouds. We choose to use an AMF that only accounts for viewing geometry (AMF$_{trop,geo}$) due to uncertainties in the modelled vertical distribution of NO$_2$ in the UT (Stavrakou et al., 2013; Travis et al., 2016) and representation errors from a model at coarser resolution (~100 km) than TROPOMI (< 10 km at nadir). Choi et al. (2014) found that OMI partial NO$_2$ columns calculated with AMF$_{trop,geo}$ above optically thick clouds in the mid-troposphere (650 hPa) were at most 14% more than those calculated with a detailed AMF that assumed clouds are near-Lambertian surfaces with albedo of 0.8 and NO$_2$ is constant with altitude. The effect of not including a temperature correction will be small in the UT where temperatures are ~220 K anyway. To confirm this, we find that GEOS-Chem cloud-sliced UT NO$_2$ calculated with the TROPOMI AMF temperature correction expression in van Geffen et al. (2019) are only 6% less than those in Figures 1-2.

We calculate VCD$_{trop}$ by first obtaining SCD$_{trop}$ as the difference between SCD$_{tot}$ from the data product and SCD$_{strat}$ calculated as the product of the reported VCD$_{strat}$ and AMF$_{strat}$:

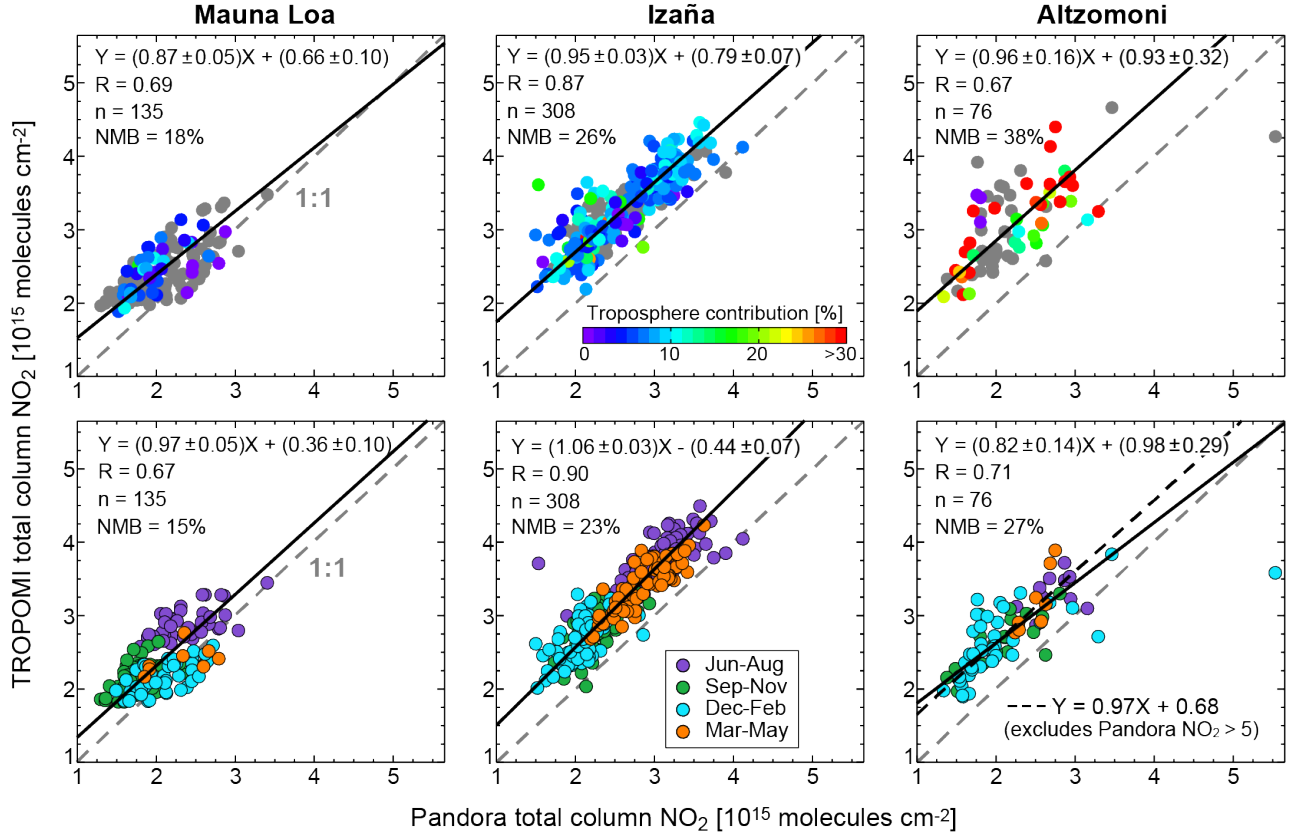$$SCD_{trop} = SCD_{tot} - (VCD_{strat} \times AMF_{strat}) \tag{1}.$$

This we use to estimate the above-cloud VCD$_{trop}$ using AMF$_{trop,geo}$ calculated with the reported solar zenith angles (SZA) and viewing zenith angles (VZA):

$$VCD_{trop} = \frac{SCD_{trop}}{AMF_{trop,geo}} = \frac{SCD_{trop}}{(\sec(SZA) + \sec(VZA))} \tag{2}.$$

The TROPOMI VCD$_{tot}$ we compare to Pandora are calculated as the sum of reported VCD$_{strat}$ and our calculated VCD$_{trop}$ (Equation (2)). Only data with quality flags ("qa_value" in the data product) of at least 0.45 are used. This removes data affected by sun glint, poor precision in the retrieval and radiances, and SZA > 84.5° (van Geffen et al., 2019). Similarly, good quality Pandora retrievals of total and tropospheric columns are identified as those with data quality flags of 0, 1, 10, or 11 (Cede et al., 2019), consistent with Ialongo et al. (2020). Coincident satellite and ground-based data are identified as TROPOMI pixels within a 0.2° radius (~20 km) of the station and ground-based data ±30 min around the TROPOMI overpass.

The upper panel of Figure 3 compares collocated daily mean Pandora and TROPOMI total columns. Errors on the daily means, obtained by adding in quadrature reported uncertainties of individual columns, are small at all sites. These vary from 0.1% to 19% for Pandora and 1.5% to 16% for TROPOMI. TROPOMI and Pandora total columns are temporally consistent (R = 0.69 at Mauna Loa, R = 0.87 at Izaña, R = 0.67 at Altzomoni), but there is a systematic positive offset in TROPOMI ranging from 6.6×10^{14} molecules cm^{-2} at Mauna Loa to 9.3×10^{14} molecules cm^{-2} at Altzomoni and TROPOMI is on average 18% higher than Pandora at Mauna Loa, 26% at Izaña, and 38% at Altzomoni. Verhoelst et al. (2020) also report a positive bias in TROPOMI total columns at the same Pandora sites of 6% at Mauna Loa, 19% at Izaña, and 28% at Altzomoni for April 2018

to February 2020. Our higher values compared to Verhoelst et al. (2020) is because of the 10% downscaling we apply to Pandora total columns. The difference in sampling footprints of space- and ground-based instruments can influence agreement between the two (Pinardi et al., 2020). We find though that the difference between TROPOMI and Pandora at Mauna Loa and Izaña is relatively unchanged by the choice of sampling coincidence. The difference is 17-20% at Mauna Loa and 25-26% at Izaña for a TROPOMI sampling radius of 0.05-0.3° and for a Pandora sampling time window of ±15-60 min. The comparison at Altzomoni though is very sensitive to the sampling radius due to proximity to Mexico City. There the difference increases from 22% at 0.05° for 45 coincident points to 48% at 0.3° for 76 coincident points.

Figure 3: Comparison of TROPOMI and Pandora total NO$_2$ columns at high-altitude sites. Points are daily means with at least 5 coincident observations at Mauna Loa (left), Izaña (centre), and Altzomoni (right) before (upper) and after (lower) applying correction factors to TROPOMI stratospheric and tropospheric columns (see text for details). Upper panel colours are the relative contribution of the troposphere to the total column according to Pandora where available, grey otherwise. Data in the lower panel are coloured by season. Lines are the 1:1 relationship (grey dashed) and RMA regression (black solid). Values inset are Pearson's correlation coefficients, RMA regression statistics, number of data points (n), and the TROPOMI normalized mean bias (NMB). Also shown for Altzomoni (bottom right panel) is the RMA regression without the Pandora > 5 × 10^{15} molecules cm^{-2} (black dashed line). Axes do not start at the origin.

At Mauna Loa, the tropospheric column contribution to the total averages 5.1% (range of 0.2-16%), according to Pandora, compared to 8.3% (0.2-38%) at Izaña and 31% (8-91%) at Altzomoni. We thus use Mauna Loa total columns to identify that
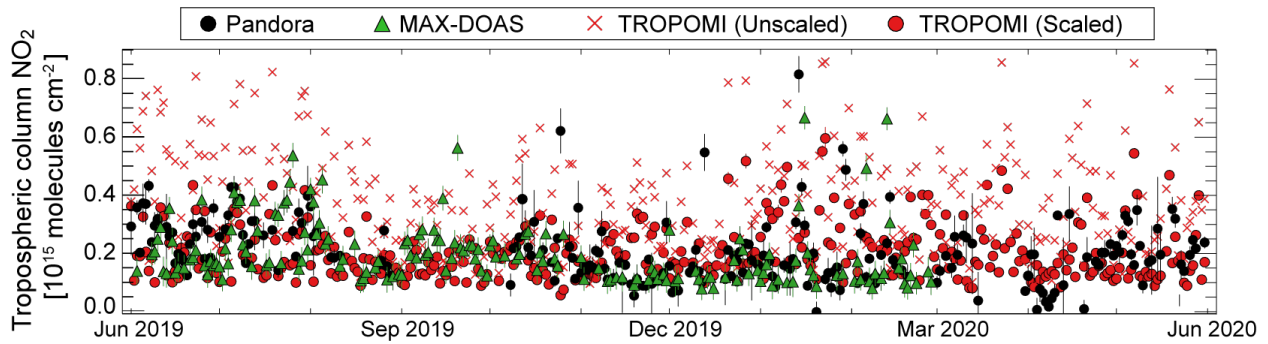
TROPOMI underestimates stratospheric NO_2 variance by 13% (slope = 0.87 ± 0.05). This is likely because the variability in stratospheric NO_2 is smoothed by the coarser spatial resolution of the TM5-TMP model ($1° \times 1°$) and time resolution of the meteorology (3-hourly). The underestimate in stratospheric NO_2 variance would lead to an overestimate in the relative contribution of the stratosphere to the total column for small column densities and vice versa. The impact on the cloud-sliced

330 UT NO_2 is steep regression slopes and an overestimate in cloud-sliced UT NO_2, as the upper troposphere column density will be overestimated for high-altitude clouds and underestimated for low-altitude clouds. The 18% higher TROPOMI than Pandora total columns at Mauna Loa is larger than and opposite in sign to the <10% (-2×10^{14} molecules cm^{-2}) meridional difference in TROPOMI stratospheric columns from the near-real time (NRTI) NO_2 product and those obtained with twilight measurements from the near-global Système d'Analyse par Observation Zénitale (SAOZ) network of Zenith Scattered Light

335 Differential Optical Absorption Spectroscopy (ZSL-DOAS) instruments (Lambert et al., 2019). The implied difference between SAOZ and Pandora stratospheric columns coincident with TROPOMI (Pandora < SAOZ) may be due to the need to account for time differences between the SAOZ measurements (twilight) and TROPOMI (midday) (Verhoelst et al., 2020). This difference warrants further investigation, as these ground-based measurements are crucial for validating space-based sensors that measure NO_2.

340

The underestimate in TROPOMI stratospheric column variance may contribute to the general pattern in validation studies comparing TROPOMI and Pandora total columns that find TROPOMI is less than Pandora when NO_2 is large and more than Pandora when NO_2 is small for the global Pandora network (Pinardi et al., 2020; Verhoelst et al., 2020) and at individual Pandora sites. TROPOMI is less than Pandora (-24 to -28%) at a relatively polluted Greater Toronto Area site, but more than

345 Pandora (8-11%) at a cleaner rural site north of the city (X. Zhao et al., 2020). Similarly, at a site in Helsinki, Finland, TROPOMI is less than Pandora (-28%) for Pandora > 10×10^{15} molecules cm^{-2} and more than Pandora (17%) for Pandora < 10×10^{15} molecules cm^{-2} (Ialongo et al., 2020).

After applying the stratospheric NO_2 variance correction, the intercepts in the top panel of Figure 3 decrease to 4.4×10^{14}

350 molecules cm^{-2} for Mauna Loa, 7.9×10^{14} molecules cm^{-2} for Izaña, and 7.3×10^{14} molecules cm^{-2} for Altzomoni (not shown). Likely causes for the remaining discrepancy between TROPOMI and Pandora include a positive offset in the TROPOMI radiance intensity that is 5% of the total column or $0.1-1 \times 10^{15}$ molecules cm^{-2} (van Geffen et al., 2020), challenges obtaining a Pandora reference measurement (atmospheric column without NO_2) (Herman et al., 2009), and an overestimate in TROPOMI free tropospheric NO_2. The radiance intensity offset has been shown to mostly affect retrievals over open oceans (van Geffen

355 et al., 2020), and an overestimate in free tropospheric NO_2 would have a larger effect on the total column comparison at Izaña and Altzomoni than at Mauna Loa.

Figure 4: Time series of free tropospheric column NO₂ at Izaña. Points are daily midday means from Pandora (black circles), MAX-DOAS (green triangles), and TROPOMI (red) before (crosses) and after (circles) applying scaling factors to the stratospheric and tropospheric columns (see text for details). Error bars are individual retrieval uncertainties added in quadrature.

Figure 4 compares time series of free tropospheric NO₂ at Izaña from Pandora, MAX-DOAS and TROPOMI. As with the total columns, Pandora and MAX-DOAS are sampled 30 min around the satellite overpass and TROPOMI 0.2° around the site. We impose a modest threshold to sample TROPOMI tropospheric columns $>4 \times 10^{13}$ molecules cm⁻² to mimic the detection limits of the instruments (Gomez et al., 2014) and mitigate the influence of TROPOMI data that would be susceptible to errors in distinguishing the stratosphere from the troposphere. This brings the lower-end TROPOMI values into better agreement with the ground-based values and has no effect on TROPOMI columns $>2 \times 10^{14}$ molecules cm⁻². On average, Pandora is 14% more than MAX-DOAS and the temporal correlation is modest (R = 0.4). Temporal inconsistencies between Pandora and MAX-DOAS are due to challenges retrieving tropospheric columns routinely close to instrument detection limits (Gomez et al., 2014), lack of dynamic variability in the retrieved columns, and differences in the sampling extent of the two instruments. The MAX-DOAS sampling footprint, for example, shifts by at least 2° in latitude between winter and summer solstices (Robles-Gonzalez et al., 2016). Most MAX-DOAS and Pandora data are at $1-4 \times 10^{14}$ molecules cm⁻², whereas the range for TROPOMI calculated using Eq. (1) and (2) extends to $\sim 8 \times 10^{14}$ molecules cm⁻². P. Wang et al. (2020a) obtained the same range in tropospheric column densities from comparison of TROPOMI to shipborne MAX-DOAS measurements. They found that TROPOMI was on average 4×10^{14} molecules cm⁻² more than MAX-DOAS. In our comparison, TROPOMI free tropospheric columns (red crosses in Figure 4) are 77% more than Pandora and 84% more than MAX-DOAS. A similar overestimate is obtained if the reported detailed tropospheric AMF is used instead of $AMF_{trop,geo}$ (Eq. (2)) to calculate TROPOMI tropospheric columns. The stratospheric variance correction reduces the difference between TROPOMI and the ground-based measurements to 40% compared to Pandora and 47% compared to MAX-DOAS due to an increase in the relative contribution of the stratosphere to total columns $> 2 \times 10^{15}$ molecules cm⁻². To address the remaining difference between TROPOMI tropospheric columns and the ground-based observations, we downscale TROPOMI tropospheric columns by 50% (red circles in Figure 4) leading to a difference of -4% with Pandora and 1% with MAX-DOAS. There is no temporal correlation between daily coincident observations of TROPOMI and the ground-based measurements (R < 0.1), consistent with the comparison of TROPOMI to shipborne MAX-DOAS by P. Wang et al. (2020a).

13

The lower panel in Figure 3 compares Pandora to TROPOMI total columns after increasing TROPOMI stratospheric column variance by 13% and reducing TROPOMI tropospheric columns by 50%. This correction reduces the difference between TROPOMI and Pandora by just 3 percentage points at Mauna Loa and Izaña and 11 percentage points at Altzomoni. The variance at Altzomoni degrades from 0.96 ± 0.16 to 0.82 ± 0.14, but this is because the relatively few coincident points (76 compared to 308 at Izaña) are influenced by the single Pandora observation $>5.5 \times 10^{15}$ molecules cm^{-2} (coincident corrected TROPOMI is $< 4 \times 10^{15}$ molecules cm^{-2}) that may be detecting NO$_2$ from fires typical of December-February in the National Park where the instrument is located (Bravo et al., 2002; Baumgardner et al., 2009). The TROPOMI tropospheric column contribution at Mauna Loa and Izaña is more consistent with that from Pandora after applying the stratospheric and tropospheric column corrections, decreasing from 8% to 6% at Mauna Loa and 12% to 7% at Izaña. This is not the case for Altzomoni (decrease from 14% to 9%), due to anthropogenic influence from Mexico City. Points in Figure 3 are coloured by season to show that all sites experience a modest decline in NO$_2$ from summer (purple) to winter (cyan) due to the influence of solar variability on photochemical production of NO$_x$ in the stratosphere (Gil et al., 2008; Robles-Gonzalez et al., 2016) and seasonality in long-range transport and subsidence in the free troposphere (Gil-Ojeda et al., 2015). The distinct distribution of points in December-February compared to June-August and September-November at Mauna Loa suggest there may be seasonality in the size of the discrepancy between TROPOMI and Pandora stratospheric columns. The remaining TROPOMI positive offset of $\sim 4 \times 10^{14}$ molecules cm^{-2} is consistent with the $2\text{-}4 \times 10^{14}$ molecules cm^{-2} positive offset in TROPOMI stratospheric columns reported by P. Wang et al. (2020a) from comparison to shipborne MAX-DOAS measurements. If the remaining offset is exclusively due to the stratospheric column, this would cancel in the cloud-slicing retrieval for clusters of partial columns with uniform stratospheric NO$_2$.

4 Retrieval of TROPOMI NO$_2$ in the upper troposphere

The same cloud-slicing retrieval steps applied to synthetic spectra from GEOS-Chem (Section 2) are applied to corrected TROPOMI total columns to obtain seasonal mean UT NO$_2$ for a year (June 2019 to May 2020) at $1° \times 1°$. This resolution degrades TROPOMI nadir pixels by 400-fold compared to 250-fold for the synthetic experiment in Section 2 and a much greater (1300-fold) degradation in OMI nadir pixel resolution (13 km $\times$ 24 km) for the $5° \times 8°$ product (Marais et al., 2018). The finer relative resolution we choose for TROPOMI cloud-sliced UT NO$_2$ compared to OMI is informed by the synthetic experiment applied to GEOS-Chem and the superior cloud-resolving capability of TROPOMI than OMI. Cloud-slicing is applied to partial columns above optically thick clouds (diagnosed with an effective cloud fraction ≥ 0.7, as in Marais et al. (2018)) to limit contamination from light transmitted through clouds. Though the cloud-slicing retrieval steps applied to GEOS-Chem and TROPOMI are the same, there are differences in the modelled and retrieved cloud parameters that we discuss below.

Two TROPOMI cloud-sliced UT NO_2 products are derived using cloud top heights and cloud fractions from distinct cloud products. These are FRESCO-S from the same data file as TROPOMI NO_2 and the standalone offline (OFFL) cloud product. FRESCO-S cloud fractions and cloud top pressures are determined by minimizing the difference between measured and simulated spectra in the O_2 A-band (758-766 nm) using lookup tables of relevant physical parameters and assuming clouds are single layer Lambertian reflectors with albedo of 0.8 (P. Wang et al., 2008; van Geffen et al., 2019). The standalone product version number changes from 01-01-07 to 01-01-08 on 7 March 2020, but with no change to the data product (Argyrouli et al., 2019). Cloud fractions are from the Optical Cloud Recognition Algorithm (OCRA). In OCRA, cloud fractions are retrieved by determining the difference, in colour space, between cloudy and clear reflectances in blue (405-495 nm) and green (350-395 nm) broad spectral bands (Loyola et al., 2007; 2018a; 2018b). Cloud top heights (in km) are from the Retrieval of Cloud Information using Neural Networks (ROCINN). This involves minimizing the difference between measured O_2 A-band radiances and neural network trained radiances modelled using OCRA cloud fractions as input (Loyola et al., 2007; 2018b) and assuming clouds are multiple optically uniform layers of light-scattering water droplets (the clouds-as-layers or CAL model). We convert ROCINN-CAL cloud top heights to pressures for cloud-slicing and comparison to FRESCO-S. FRESCO-S data are quality screened using the same qa_value threshold (0.45) as the NO_2 data. A qa_value threshold of 0.5 is used for OCRA cloud fractions and ROCINN-CAL cloud heights. This removes data affected by sun glint, spectral saturation that is particularly problematic over bright high-altitude clouds and not properly flagged in the level 1 radiances used to retrieve NO_2 slant columns (Gorkavyi et al., 2020), poor quality radiances and retrievals, SZA > 75°, and issues arising from spatial misalignment of ground pixels of different spectral bands (Loyola et al., 2018a; 2018b). Snow/ice scenes that could be misidentified as clouds in the FRESCO-S product are identified as scenes with differences in reported scene and surface pressures > 2% (as in van der A et al. (2020)), snow cover > 80% or permanent ice cover. Snow and ice cover and classification are from the Near-real-time Ice and Snow Extent (NISE) product provided with the NO_2 product (van Geffen et al., 2019). For OCRA and ROCINN-CAL, we use the reported snow/ice flag that combines information from NISE and a surface albedo climatology (Loyola et al., 2018b). In what follows, we distinguish the two cloud-sliced TROPOMI UT NO_2 products as FRESCO-S UT NO_2 and ROCINN-CAL UT NO_2.
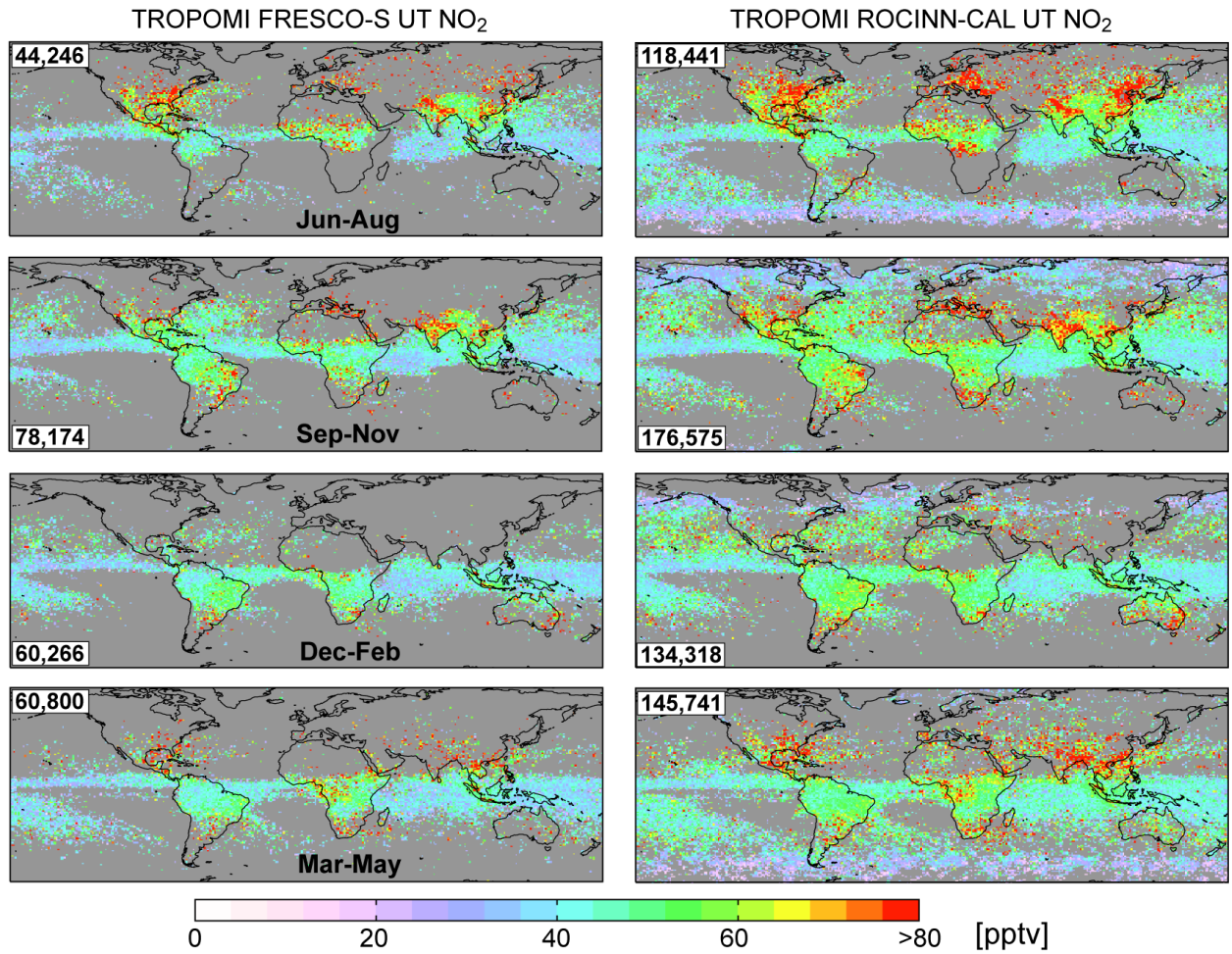
Figure 5: Seasonal mean upper tropospheric (UT) NO₂ from TROPOMI. Maps are UT NO₂ at 1° × 1° in June-August 2019 (first row), September-November 2019 (second), December 2019 to February 2020 (third), and March-May 2020 (fourth) using FRESCO-S (left) or ROCINN-CAL (right) cloud information and with corrections applied to TROPOMI stratospheric and tropospheric columns (see text for details). Inset numbers give total successful cloud-sliced retrievals. Grey grid squares have fewer than 5 cloud-sliced retrievals.

Figure 5 shows maps of seasonal mean FRESCO-S and ROCINN-CAL UT NO₂ at 1° × 1°. The spatial features are consistent with a combination of the density of lightning flashes (Cecil et al., 2014) and lightning properties such as flash footprint, duration, and energy (Beirle et al., 2014). These include elevated concentrations (> 80 pptv) over northern hemisphere land masses in June-August, the year-round 40-60 pptv band over tropical landmasses that shifts meridionally with the Intertropical Convergence Zone (ITCZ), and relatively low concentrations (< 30 pptv) over the remote Pacific Ocean. In the cold polar regions UT NO₂, limited to ROCINN-CAL, are near-background (<30 pptv; Marais et al. (2018)) as NO₂ is preferentially present as NOₓ reservoir compounds such as peroxyacetyl nitrates (PANs) (Bottenheim et al., 1986). Large enhancements (NO₂ > 80 pptv) over northern China and the northeast US in June-August, and Australia in December-February most prevalent in the ROCINN-CAL product likely reflect contamination from surface pollution below clouds. These would result from

16

intense anthropogenic activity in North China and the northeast US (B. Zhao et al., 2013; Jiang et al., 2018; Z. Wang et al., 2020b) and routine pyrocumulonimbus injection of fire plumes into the free troposphere and lower stratosphere during the intense 2019-2020 fire season in Australia (Kablick III et al., 2020). Coincident gridsquares of the two data sets are spatially consistent (R of 0.82 to 0.88), though ROCINN-CAL UT NO_2 are 4.2-9.1 pptv more than FRESCO-S UT NO_2. As with the synthetic experiment, UT NO_2 increases with degradation in resolution. Depending on the season, cloud-sliced UT NO_2 are 2-4% more at $2° \times 2.5°$ and 3-9% more at $4° \times 5°$ than at $1° \times 1°$. Good quality retrievals and optically thick clouds with cloud top pressures at 450-180 hPa account for ~2% of TROPOMI pixels using FRESCO-S and ~3% using ROCINN-CAL. Of these, 44,000-78,000 cloud-slicing retrievals are retained in each season for FRESCO-S, and 118,000-177,000 for ROCINN-CAL (Figure 5). Most data loss in the cloud-slicing retrieval is because of too few points (clusters < 10) or cloud top pressure range < 140 hPa. Discarded extreme values of cloud-sliced NO_2 > 200 pptv are only 0.1-0.5% of retained data. More cloud-sliced retrievals with ROCCIN-CAL is due to greater abundance of optically thick clouds and clusters with greater cloud height range.
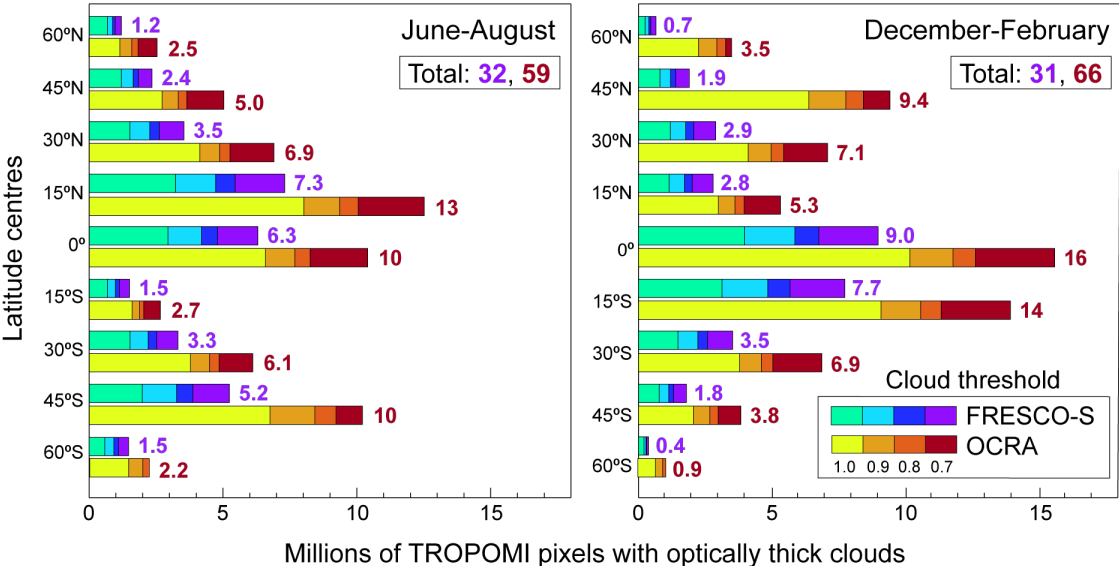
Figure 6 compares the meridional abundance of optically thick clouds in the UT from the two cloud products for June-August and December-February. The same information for the other two seasons is in Figure S2. Both products retrieve effective (radiometric) cloud fractions. These are systematically less than the physical (geometric) cloud fractions from GEOS-Chem, though the two converge for optically thick clouds with physical cloud fractions approaching 1 (Stammes et al., 2008). The number of OCRA optically thick clouds is always more (often double) than that of FRESCO-S in all seasons and across all latitudes. The greatest difference in the number of optically thick clouds tracks the ITCZ and is also typically at 45°N/S. The majority (61-62%) of OCRA cloud fractions exceed 0.975 compared to 42-45% for FRESCO-S. Loyola et al. (2018a) determined that OCRA cloud fractions retrieved over oceans are 0.1 unit more than those from retrievals like FRESCO-S that assume fixed cloud albedo. Differences over land are not as systematic and vary from negligible in the tropics and subtropics to > 0.1 unit more in the Arctic (Loyola et al., 2018a). The OCRA algorithm ordinarily includes red band reflectances, but TROPOMI OCRA relies on initial cloud-free reflectances from OMI that excludes the red part of the visible spectrum, though its absence only induces a small negative cloud fraction bias of ~0.03 (Loyola et al., 2018a). ROCINN-CAL retrieves cloud optical thicknesses alongside cloud heights. These exceed 20 for most (84-93%) $1° \times 1°$ gridsquares used to cloud-slice TROPOMI, confirming that a cloud fraction threshold of 0.7 is sufficient to isolate optically thick clouds. The number of pixels in each cloud fraction threshold in Figure 6 suggests that a stricter cloud fraction threshold of 1.0 applied to the ROCINN-CAL product might lead to a more consistent spatial distribution of UT NO_2 to that from FRESCO-S in Figure 5. The resultant ROCINN-CAL UT NO_2 using a cloud fraction threshold of 1.0 are in Figure S3. Half the number of cloud-sliced retrievals are obtained, as expected, and there are fewer retrievals over northern hemisphere high latitudes than in Figure 5. Those over the southern ocean in austral autumn and winter persist and may reflect enhanced occurrence of high-altitude clouds in these seasons over Antarctica (Verlinden et al., 2011). The average difference between ROCINN-CAL and FRESCO-S decreases
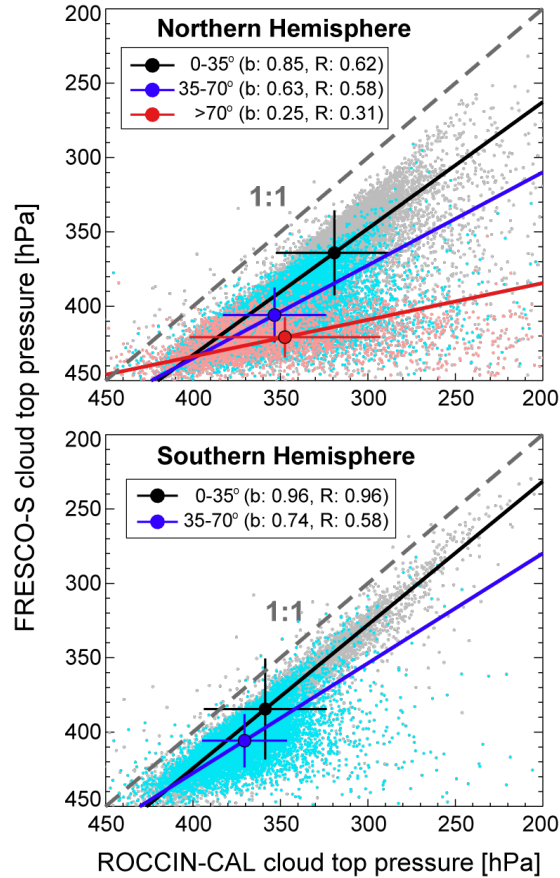
490   from 5-8% for the same cloud fraction threshold of 0.7 to 0.2-1.6% using a cloud fraction threshold of 1.0 for ROCINN-CAL and 0.7 for FRESCO-S.

Figure 6: Meridional distribution of FRESCO-S and OCRA optically thick clouds in the upper troposphere. Bars count the
495   **occurrence of native TROPOMI pixels with cloud fractions ≥ 1.0, 0.9, 0.8, and 0.7 binned into 15° latitude bands in June-August (left) and December-February (right) for FRESCO-S (cool colours) where FRESCO-S cloud top pressures are at 450-180 hPa, and OCRA (warm colours) where ROCINN-CAL cloud top pressures are at 450-180 hPa. Values inset are latitude band and global total number of TROPOMI pixels with cloud fraction ≥ 0.7.**
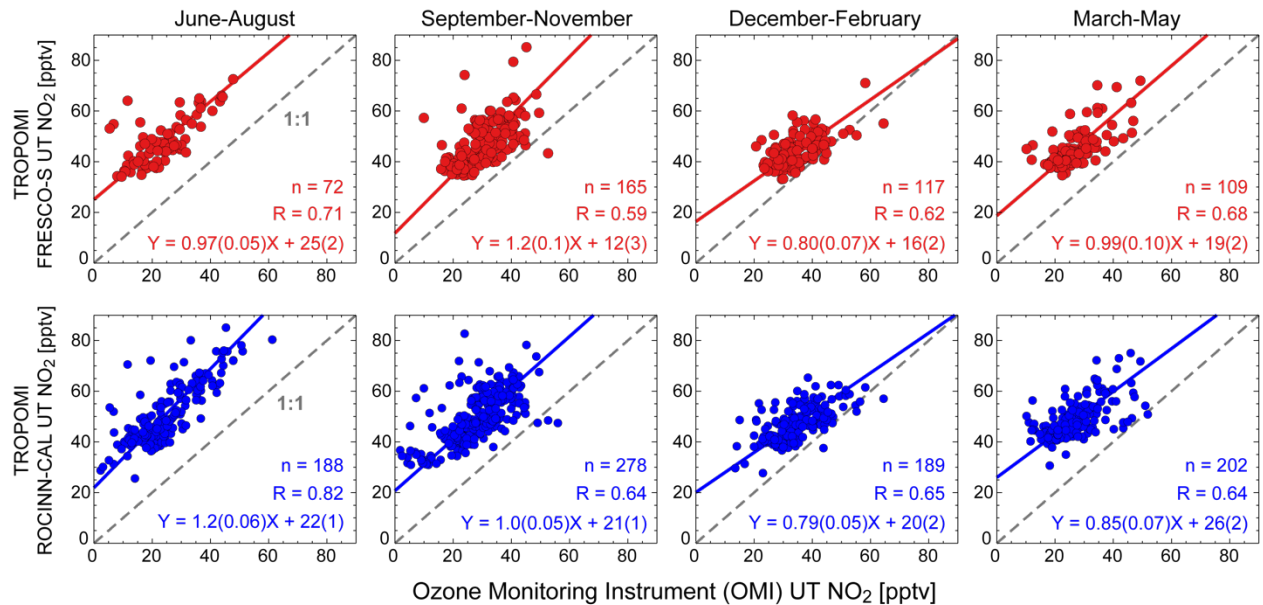
Figure 7 compares gridded cloud product cloud top pressures for June-August sampled where FRESCO-S cloud top pressures
500   are at 450-180 hPa and cloud fractions are at least 0.7. Cloud top pressures are spatially consistent in the tropics (R = 0.62 at 0-35°N, R = 0.85 at 0-35°N) and midlatitudes (R = 0.58 at 35-70°N, R = 0.63 at 35-70°S), but degrade north of 70°N (R = 0.31). Variability in cloud top pressures is similar for the two products in the tropics (regional mean standard deviation of 28-33 hPa at 0-35°N and 30-31 hPa at 0-35°S), but deviates in the subtropics and midlatitudes (18 hPa for FRESCO-S, 24-30 hPa for ROCINN-CAL) and more so in the Arctic (13 hPa for FRESCO-S, 54 hPa for ROCINN-CAL). There is no coincident data
505   south of 70°S in June-August. In December-February south of 70°S (Figure S4) there is a similarly weak correlation (R < 0.1) and large difference in variability (19 hPa for FRESCO-S, 80 hPa for ROCINN-CAL). FRESCO-S does not account for scattering within and below clouds and so estimates the height as the optical centroid of the cloud (Joiner et al., 2012). The optical centroid is systematically lower in altitude (higher in pressure) than the physical cloud top, though FRESCO-S appears to be more consistent with ground-based observations than ROCINN-CAL for high-altitude cloud top heights (Compernolle
510   et al., 2020). Loyola et al. (2018a) determined that cloud top altitudes from ROCINN-CAL were ~1 km (range: 0.6 km to >2 km) higher than those from a FRESCO-S type approach that assumes clouds are single layers with fixed albedo. Our test of the effect of an artificial decrease in cloud top altitude of 1 km for cloud-slicing synthetic GEOS-Chem partial columns (Section

18

2) suggests that 1 km lower altitude cloud tops in FRESCO-S should lead to larger UT NO_2 than those from ROCINN-CAL, but the opposite is observed (Figure 5). This suggests that the effect of other differences between the cloud products on the cloud-sliced UT NO_2 must dominate. Regression slopes in Figure 7 are less than unity, indicating that the difference in cloud top pressures between the two products decreases with pressure (increases with altitude). The implication for cloud-sliced UT NO_2 is greater global coverage with ROCINN-CAL, as clusters of TROPOMI pixels in the midlatitudes and polar regions overcome the 140 hPa cloud top pressure range threshold imposed in the cloud-slicing algorithm. In the tropics and subtropics, ROCINN-CAL has less cloud top pressure range than FRESCO-S for the same scenes. This leads to steeper cloud-slicing regression slopes for ROCINN-CAL and explains the 4-9 pptv greater UT NO_2 than FRESCO-S in Figure 5.

Figure 7: Comparison of FRESCO-S and ROCINN-CAL cloud top pressures from optically thick clouds in the upper troposphere for June-August 2019. Data are gridded to 1° × 1° for TROPOMI pixels with FRESCO-S cloud fractions ≥ 0.7 and cloud top pressures at 450-180 hPa. Small points are gridded seasonal means and lines are RMA regressions for the tropics (grey points, black regression line), subtropics and midlatitudes (cyan, blue), and the Arctic (pink, red). Large points are latitude band means and error bars are corresponding standard deviations. Grey dashed lines show the 1:1 relationship. Values in the legend are RMA regression slopes (b) and Pearson's correlation coefficients (R).

5 Comparison of TROPOMI and OMI UT NO₂

We evaluate TROPOMI UT NO2 with multiyear (2005-2007) seasonal mean cloud-sliced UT NO2 from OMI at 5° × 8° (Marais et al., 2018). The OMI product is retrieved in a similar manner to TROPOMI, except that the GMI CTM is used to diagnose and remove steep gradients in NO2 ($\geq$ 0.33 pptv hPa^{-1}) and the OMI retrieval ceiling is lower (280 hPa, ~10 km) than TROPOMI (180 hPa, ~12.5 km). In regions where lightning is prevalent, the vertical distribution of NO2 increases with altitude by 10-50 pptv across 280-180 hPa, as is observed with vertical profiles of NO2 from spring-summer research aircraft campaign measurements over the US (Boersma et al., 2011; Silvern et al., 2018). Strict filtering applied to cloud-slicing removes most scenes where the increase in NO2 with altitude exceeds 33 pptv across 280-180 hPa, based on the synthetic experiment with GEOS-Chem. The influence of more than a 10-year gap between the OMI and TROPOMI UT NO2 datasets on the comparison is challenging to quantify, due to paucity of routine measurements of NO2 in the UT. The contribution of changes in lightning activity should be small, as interannual variability is small (<5%) and there is no discernible trend in the long-term record of satellite observations of lightning flashes (Schumann and Huntrieser, 2007).

Figure 8: Comparison of TROPOMI and OMI cloud-sliced UT NO₂. Points are seasonal means in June 2019 to May 2020 for TROPOMI and January 2005 to December 2007 for OMI gridded to the same 5° × 8° (latitude × longitude) grid for FRESCO-S vs OMI (upper panel, red) and ROCINN-CAL vs OMI (lower panel, blue). Values give the number of points, Pearson's correlation coefficients (R), RMA regression coefficients, and, in parentheses, bootstrap resampling slope and intercept errors.

Figure 8 evaluates spatial consistency between TROPOMI and OMI seasonal mean UT NO2 on the OMI grid (5° × 8°) for TROPOMI cloud-sliced UT NO2 1° × 1° gridsquares with at least 10 cloud-sliced retrievals. TROPOMI is spatially consistent with OMI in all seasons for both products (R = 0.6-0.8). The TROPOMI background is 12-25 pptv more than OMI for FRESCO-S and 20-26 pptv more than OMI for ROCINN-CAL, based on the intercepts in Figure 8. This may be due to the

observed increase in NO$_2$ with altitude across the sampling pressure ceilings of the two products (280 hPa for OMI, 180 hPa for TROPOMI). The OMI UT NO$_2$ product uses cloud information derived from OMI O$_2$-O$_2$ slant columns. The signal from the O$_2$-O$_2$ dimer declines with altitude, increasing uncertainty in the retrieval with altitude (Veefkind et al., 2016). High-altitude clouds from OMI would have to be higher in altitude than TROPOMI to contribute to the positive offset in TROPOMI UT NO$_2$ in Figure 8, based on results from the synthetic test of lowering GEOS-Chem cloud top heights by 1 km. But the direction of the bias in OMI high-altitude cloud top heights compared to lidar-radar measurements does not appear to be systematic (Veefkind et al., 2016). The regression slopes in Figure 8 are closest to unity for June-August and March-May for FRESCO-S and September-November for ROCINN-CAL. The underestimate in variance in December-February in both products could reflect the need to account for seasonality in the stratospheric variance correction. UT NO$_2$ obtained without applying correction factors to TROPOMI stratospheric and tropospheric columns (Figure S5) results in greater data density due to less variance in TROPOMI stratospheric columns, but the discrepancy with OMI is much greater. TROPOMI UT NO$_2$ background concentrations are 16-35 pptv more than OMI for FRESCO-S and 27-36 pptv more for ROCINN-CAL and slopes exceed unity in all seasons (1.3-1.7 for FRESCO-S, 1.2-1.5 for ROCINN-CAL).

6 Conclusions

We have developed new products of NO$_2$ in the upper troposphere (UT; ~8-12 km) by cloud-slicing partial columns of NO$_2$ from the space-based TROPOMI instrument. This involves regressing partial NO$_2$ columns against cloud top pressures and converting regression slopes to UT NO$_2$ mixing ratios.

We first refined and tested representativeness of cloud-sliced UT NO$_2$ by applying cloud-slicing to synthetic partial columns from the GEOS-Chem model. Synthetic cloud-sliced UT NO$_2$ are spatially consistent (R = 0.64) with the synthetic truth, but preferentially sampling cloudy scenes and substantial data loss lead to a resolution-dependent positive bias in cloud-sliced UT NO$_2$ of 11-22%.

Before applying cloud-slicing to TROPOMI, we evaluated TROPOMI with Pandora total columns at high-altitude sites (Mauna Loa, Izaña, Altzomoni) and Pandora and MAX-DOAS free tropospheric columns at Izaña. We identified discrepancies between TROPOMI and ground-based NO$_2$ measurements that include a 13% underestimate in TROPOMI stratospheric NO$_2$ variance and 50% overestimate in TROPOMI tropospheric columns.

We retrieved UT NO$_2$ from TROPOMI by applying the refined cloud-slicing algorithm to corrected TROPOMI partial columns above optically thick clouds with cloud top heights at 450-180 hPa using two alternate cloud products, FRESCO-S and ROCINN-CAL. ROCINN-CAL UT NO$_2$ has more extensive coverage (0°-70° N/S) than FRESCO-S (0°-45° N/S) due to its greater abundance of optically thick clouds. Coincident UT NO$_2$ from the two products exhibit similar spatial distribution, but

background UT NO_2 from ROCINN-CAL is 4-9 pptv more than FRESCO-S. This is due to steeper cloud-slicing regression slopes for ROCINN-CAL, as cloud top heights between the two products deviate with increasing cloud top pressure. Ongoing validation studies are needed to resolve these differences.

Both products are spatially correlated with the existing coarse resolution (5° latitude × 8° longitude) Ozone Monitoring Instrument (OMI) product, except that TROPOMI is 16-36 pptv more than OMI that we reason is due to the widely documented increase in NO_2 with altitude from the OMI pressure ceiling (280 hPa) to that for TROPOMI (180 hPa), but signal saturation of TROPOMI pixels leading to blooming over bright high-altitude clouds could also contribute.

TROPOMI UT NO_2 products presented here have the potential to provide routine, extensive and consistent measurements of NO_x in the UT and, as TROPOMI observations accumulate, aid in characterising interannual and long-term variability in NO_x in the under sampled UT.

Code Availability

Python code used to process TROPOMI data is available at https://doi.org/10.5281/zenodo.4058442.

Data Availability

Data can be requested from EAM for TROPOMI UT NO_2, SC for OMI UT NO_2, MN-C for MAX-DOAS slant columns, and RR for MAX-DOAS vertical columns. Python code used to process TROPOMI data is available at https://doi.org/10.5281/zenodo.4058442.

Author Contributions

EAM led the analysis and writing, simulated GEOS-Chem, and cloud-sliced TROPOMI UT NO_2 and GEOS-Chem. JFR refined and documented python processing code. RGR retrieved MAX-DOAS vertical tropospheric columns. HE and FB provided guidance on best use and evaluation of TROPOMI NO_2. SC and JJ retrieved OMI UT NO_2 and provided guidance on cloud-slicing. NA and AR are Pandora site PIs, and AC is PI of PGN. MNC maintains the RASAS-II instrument and retrieved the MAX-DOAS slant columns at Izaña. LG conducted MAX-DOAS geospatial sampling sensitivity tests for Izaña.

Competing Interests

The authors declare that they have no conflict of interest.

References

Allen, D., Pickering, K., Duncan, B., and Damon, M.: Impact of lightning NO emissions on North American photochemistry as determined using the Global Modeling Initiative (GMI) model, J. Geophys. Res.-Atmos., 115, 1-24, doi:10.1029/2010jd014062, 2010.

Amedro, D., Bunkan, A. J. C., Berasategui, M., and Crowley, J. N.: Kinetics of the OH + NO_2 reaction: rate coefficients (217-333 K, 16-1200 mbar) and fall-off parameters for N_2 and O_2 bath gases, Atmos. Chem. Phys., 19, 10643-10657, doi:10.5194/acp-19-10643-2019, 2019.

Argyrouli, A., Sneep, M., and Lambert, J.-C.: S5P Mission Performance Centre CLOUD [L2__CLOUD_] Readme, https://sentinel.esa.int/documents/247904/3541451/Sentinel-5P-Cloud-Level-2-Product-Readme-File (Last accessed: 20 January 2020), 2019.

Baumgardner, D., Grutter, M., Allan, J., Ochoa, C., Rappenglueck, B., Russell, L. M., and Arnott, P.: Physical and chemical properties of the regional mixed layer of Mexico's Megapolis, Atmos. Chem. Phys., 9, 5711-5727, doi:10.5194/acp-9-5711-2009, 2009.

Beirle, S., Koshak, W., Blakeslee, R., and Wagner, T.: Global patterns of lightning properties derived by OTD and LIS, Nat. Hazard Earth Sys., 14, 2715-2726, doi:10.5194/nhess-14-2715-2014, 2014.

Belmonte-Rivas, M. B., Veefkind, P., Eskes, H., and Levelt, P.: OMI tropospheric NO_2 profiles from cloud slicing: constraints on surface emissions, convective transport and lightning NO_x, Atmos. Chem. Phys., 15, 13519-13553, doi:10.5194/acp-15-13519-2015, 2015.

Bertram, T. H., Perring, A. E., Wooldridge, P. J., Crounse, J. D., Kwan, A. J., Wennberg, P. O., Scheuer, E., Dibb, J., Avery, M., Sachse, G., Vay, S. A., Crawford, J. H., McNaughton, C. S., Clarke, A., Pickering, K. E., Fuelberg, H., Huey, G., Blake, D. R., Singh, H. B., Hall, S. R., Shetter, R. E., Fried, A., Heikes, B. G., and Cohen, R. C.: Direct measurements of the convective recycling of the upper troposphere, Science, 315, 816-820, doi:10.1126/science.1134548, 2007.

Boersma, K. F., Eskes, H. J., and Brinksma, E. J.: Error analysis for tropospheric NO_2 retrieval from space, J. Geophys. Res.-Atmos., 109, 1-26, doi:10.1029/2003jd003962, 2004.

Boersma, K. F., Eskes, H. J., Dirksen, R. J., van der A, R. J., Veefkind, J. P., Stammes, P., Huijnen, V., Kleipool, Q. L., Sneep, M., Claas, J., Leitao, J., Richter, A., Zhou, Y., and Brunner, D.: An improved tropospheric NO_2 column retrieval algorithm for the Ozone Monitoring Instrument, Atmos. Meas. Tech., 4, 1905-1928, doi:10.5194/amt-4-1905-2011, 2011.

645   Bottenheim, J. W., Gallant, A. G., and Brice, K. A.: Measurements of NO_y species and O_3 at 82°N latitude, Geophys. Res. Lett., 13, 113-116, doi:10.1029/GL013i002p00113, 1986.

Bradshaw, J., Davis, D., Grodzinsky, G., Smyth, S., Newell, R., Sandholm, S., and Liu, S.: Observed distributions of nitrogen oxides in the remote free troposphere from the NASA global tropospheric experiment programs, Rev. Geophys., 38, 61-116, doi:10.1029/1999rg900015, 2000.

650   Bravo, A. H., Sosa, E. R., Sánchez, A. P., Jaimes, P. M., and Saavedra, R. M. I.: Impact of wildfires on the air quality of Mexico City, 1992–1999, Environ. Pollut., 117, 243-253, doi:10.1016/S0269-7491(01)00277-9, 2002.

Brohede, S. M., Haley, C. S., McLinden, C. A., Sioris, C. E., Murtagh, D. P., Petelina, S. V., Llewellyn, E. J., Bazureau, A., Goutail, F., Randall, C. E., Lumpe, J. D., Taha, G., Thomasson, L. W., and Gordley, L. L.: Validation of Odin/OSIRIS stratospheric NO_2 profiles, J. Geophys. Res.-Atmos., 112, 1-22, doi:10.1029/2006JD007586, 2007.

655   Browne, E. C., Perring, A. E., Wooldridge, P. J., Apel, E., Hall, S. R., Huey, L. G., Mao, J., Spencer, K. M., St Clair, J. M., Weinheimer, A. J., Wisthaler, A., and Cohen, R. C.: Global and regional effects of the photochemistry of $CH_3O_2NO_2$: evidence from ARCTAS, Atmos. Chem. Phys., 11, 4209-4219, doi:10.5194/acp-11-4209-2011, 2011.

Cecil, D. J., Buechler, D. E., and Blakeslee, R. J.: Gridded lightning climatology from TRMM-LIS and OTD: Dataset description, Atmos. Res., 135, 404-414, doi:10.1016/j.atmosres.2012.06.028, 2014.

660   Cede, A., Tiefengraber, M., Gebetsberger, M., and Kreuter, A.: Fiducial reference measurements for air quality: TN on PGN products "correct use" guidelines, version 1, LuftBlick, Innsbruck, Austria, https://www.pandonia-global-network.org/wp-content/uploads/2020/01/LuftBlick_FRM4AQ_PGNUserGuidelines_RP_2019009_v1.pdf (Last accessed: 4 February 2020), 2019.

Chang, W. L., Bhave, P. V., Brown, S. S., Riemer, N., Stutz, J., and Dabdub, D.: Heterogeneous atmospheric chemistry,
665   ambient measurements, and model calculations of N_2O_5: A review, Aerosol Sci. Tech., 45, 665-695, doi:10.1080/02786826.2010.551672, 2011.

Choi, S., Joiner, J., Choi, Y., Duncan, B. N., Vasilkov, A., Krotkov, N., and Bucsela, E.: First estimates of global free-tropospheric NO_2 abundances derived using a cloud-slicing technique applied to satellite observations from the Aura Ozone Monitoring Instrument (OMI), Atmos. Chem. Phys., 14, 10565-10588, doi:10.5194/acp-14-10565-2014, 2014.

670   Compernolle, S., Argyrouli, A., Lutz, R., Sneep, M., Lambert, J. C., Fjæraa, A. M., Hubert, D., Keppens, A., Loyola, D., O'Connor, E., Romahn, F., Stammes, P., Verhoelst, T., and Wang, P.: Validation of the Sentinel-5 Precursor TROPOMI cloud data with Cloudnet, Aura OMI O_2-O_2, MODIS and Suomi-NPP VIIRS, Atmos. Meas. Tech. Discuss., 2020, 1-33, doi:10.5194/amt-2020-122, 2020.

Crawford, J., Davis, D., Olson, J., Chen, G., Liu, S., Fuelberg, H., Hannan, J., Kondo, Y., Anderson, B., Gregory, G., Sachse,
675   G., Talbot, R., Viggiano, A., Heikes, B., Snow, J., Singh, H., and Blake, D.: Evolution and chemical consequences of lightning-

produced NO_x observed in the North Atlantic upper troposphere, J. Geophys. Res.-Atmos., 105, 19795-19809, doi:10.1029/2000JD900183, 2000.

Dahlmann, K., Grewe, V., Ponater, M., and Matthes, S.: Quantifying the contributions of individual NO_x sources to the trend in ozone radiative forcing, Atmos. Environ., 45, 2860-2868, doi:10.1016/j.atmosenv.2011.02.071, 2011.

680   Dirksen, R. J., Boersma, K. F., Eskes, H. J., Ionov, D. V., Bucsela, E. J., Levelt, P. F., and Kelder, H. M.: Evaluation of stratospheric NO_2 retrieved from the Ozone Monitoring Instrument: Intercomparison, diurnal cycle, and trending, J. Geophys. Res.-Atmos., 116, 1-22, doi:10.1029/2010JD014943, 2011.

Ehhalt, D. H., Rohrer, F., and Wahner, A.: Sources and distribution of NO_x in the upper troposphere at northern midlatitudes, J. Geophys. Res.-Atmos., 97, 3725-3738, doi:10.1029/91JD03081, 1992.

685   Frieß, U., Monks, P. S., Remedios, J. J., Rozanov, A., Sinreich, R., Wagner, T., and Platt, U.: MAX-DOAS O_4 measurements: A new technique to derive information on atmospheric aerosols: 2. Modeling studies, J. Geophys. Res.-Atmos., 111, 1-20, doi:10.1029/2005JD006618, 2006.

Gil, M., Yela, M., Gunn, L. N., Richter, A., Alonso, I., Chipperfield, M. P., Cuevas, E., Iglesias, J., Navarro, M., Puentedura, O., and Rodriguez, S.: NO_2 climatology in the northern subtropical region: diurnal, seasonal and interannual variability, Atmos.

690   Chem. Phys., 8, 1635-1648, doi:10.5194/acp-8-1635-2008, 2008.

Gil-Ojeda, M., Navarro-Comas, M., Gomez-Martin, L., Adame, J. A., Saiz-Lopez, A., Cuevas, C. A., Gonzalez, Y., Puentedura, O., Cuevas, E., Lamarque, J. F., Kinninson, D., and Tilmes, S.: NO_2 seasonal evolution in the north subtropical free troposphere, Atmos. Chem. Phys., 15, 10567-10579, doi:10.5194/acp-15-10567-2015, 2015.

Gomez, L., Navarro-Comas, M., Puentedura, O., Gonzalez, Y., Cuevas, E., and Gil-Ojeda, M.: Long-path averaged mixing

695   ratios of O_3 and NO_2 in the free troposphere from mountain MAX-DOAS, Atmos. Meas. Tech., 7, 3373-3386, doi:10.5194/amt-7-3373-2014, 2014.

Gorkavyi, N., Fasnacht, Z., Haffner, D., Marchenko, S., Joiner, J., and Vasilkov, A.: Detection of non-linear effects in satellite UV/Vis reflectance spectra: Application to the Ozone Monitoring Instrument, Atmos. Meas. Tech. Discuss., 2020, 1-24, doi:10.5194/amt-2020-327, 2020.

700   Henderson, B. H., Pinder, R. W., Crooks, J., Cohen, R. C., Carlton, A. G., Pye, H. O. T., and Vizuete, W.: Combining Bayesian methods and aircraft observations to constrain the $HO^. + NO_2$ reaction rate, Atmos. Chem. Phys., 12, 653-667, doi:10.5194/acp-12-653-2012, 2012.

Henderson, B. H., Pinder, R. W., Crooks, J., Cohen, R. C., Hutzell, W. T., Sarwar, G., Goliff, W. S., Stockwell, W. R., Fahr, A., Mathur, R., Carlton, A. G., and Vizuete, W.: Evaluation of simulated photochemical partitioning of oxidized nitrogen in

705   the upper troposphere, Atmos. Chem. Phys., 11, 275-291, doi:10.5194/acp-11-275-2011, 2011.

Herman, J., Cede, A., Spinei, E., Mount, G., Tzortziou, M., and Abuhassan, N.: NO_2 column amounts from ground-based Pandora and MFDOAS spectrometers using the direct-sun DOAS technique: Intercomparisons and application to OMI validation, J. Geophys. Res.-Atmos., 114, 1-20, doi:10.1029/2009jd011848, 2009.

Holmes, C. D., Bertram, T. H., Confer, K. L., Graham, K. A., Ronan, A. C., Wirks, C. K., and Shah, V.: The role of clouds in the tropospheric NO_x cycle: A new modeling approach for cloud chemistry and its global implications, Geophys. Res. Lett., 46, 4980-4990, doi:10.1029/2019GL081990, 2019.

Hönninger, G., von Friedeburg, C., and Platt, U.: Multi axis differential optical absorption spectroscopy (MAX-DOAS), Atmos. Chem. Phys., 4, 231-254, doi:10.5194/acp-4-231-2004, 2004.

Ialongo, I., Virta, H., Eskes, H., Hovila, J., and Douros, J.: Comparison of TROPOMI/Sentinel-5 Precursor NO_2 observations with ground-based measurements in Helsinki, Atmos. Meas. Tech., 13, 205-218, doi:10.5194/amt-13-205-2020, 2020.

Jaeglé, L., Jacob, D. J., Wang, Y., Weinheimer, A. J., Ridley, B. A., Campos, T. L., Sachse, G. W., and Hagen, D. E.: Sources and chemistry of NO_x in the upper troposphere over the United States, Geophys. Res. Lett., 25, 1705-1708, doi:10.1029/97gl03591, 1998.

Jiang, Z., McDonald, B. C., Worden, H., Worden, J. R., Miyazaki, K., Qu, Z., Henze, D. K., Jones, D. B. A., Arellano, A. F., Fischer, E. V., Zhu, L., and Boersma, K. F.: Unexpected slowdown of US pollutant emission reduction in the past decade, PNAS, 115, 5099, doi:10.1073/pnas.1801191115, 2018.

Joiner, J., Vasilkov, A. P., Gupta, P., Bhartia, P. K., Veefkind, P., Sneep, M., de Haan, J., Polonsky, I., and Spurr, R.: Fast simulators for satellite cloud optical centroid pressure retrievals; evaluation of OMI cloud retrievals, Atmos. Meas. Tech., 5, 529-545, doi:10.5194/amt-5-529-2012, 2012.

Jones, A., Walker, K. A., Jin, J. J., Taylor, J. R., Boone, C. D., Bernath, P. F., Brohede, S., Manney, G. L., McLeod, S., Hughes, R., and Daffer, W. H.: Technical Note: A trace gas climatology derived from the Atmospheric Chemistry Experiment Fourier Transform Spectrometer (ACE-FTS) data set, Atmos. Chem. Phys., 12, 5207-5220, doi:10.5194/acp-12-5207-2012, 2012.

Kablick III, G. P., Allen, D. R., Fromm, M. D., and Nedoluha, G. E.: Australian PyroCb smoke generates synoptic-scale stratospheric anticyclones, Geophys. Res. Lett., 47, 1-9, doi:10.1029/2020GL088101, 2020.

Lamarque, J. F., Brasseur, G. P., Hess, P. G., and Müller, J. F.: Three-dimensional study of the relative contributions of the different nitrogen sources in the troposphere, J. Geophys. Res.-Atmos., 101, 22955-22968, doi:10.1029/96JD02160, 1996.

Lambert, J.-C., Keppens, A., Hubert, D., Langerock, B., K.-U. Eichmann, Kleipool, Q., Sneep, M., Verhoelst, T., Wagner, T., Weber, M., Ahn, C., A. Argyrouli, Balis, D., Chan, K. L., Compernolle, S., Smedt, I. D., Eskes, H., Fjæraa, A. M., Garane, K., Gleason, J. F., Goutail, F., Granville, J., Hedelt, P., K.-P. Heue, Jaross, G., Koukouli, M., Landgraf, J., Lutz, R., Niemejer, S., A. Pazmiño, Pinardi, G., Pommereau, J.-P., Richter, A., Rozemeijer, N., Sha, M. K., Zweers, D. S., Theys, N., Tilstra, G., Torres, O., Valks, P., Vigouroux, C., and Wang, P.: S5P Mission Performance Centre Routine Operations Consolidated Validation Report series, Issue #02, Version 02.0.2, http://www.tropomi.eu/sites/default/files/files/publicS5P-MPC-IASB-ROCVR-02.0.2-20190411_FINAL.pdf (Last accessed: 3 February 2020), 2019.

Levelt, P. F., Joiner, J., Tamminen, J., Veefkind, J. P., Bhartia, P. K., Stein Zweers, D. C., Duncan, B. N., Streets, D. G., Eskes, H., van der A, R., McLinden, C., Fioletov, V., Carn, S., de Laat, J., DeLand, M., Marchenko, S., McPeters, R., Ziemke, J., Fu, D., Liu, X., Pickering, K., Apituley, A., González Abad, G., Arola, A., Boersma, F., Chan Miller, C., Chance, K., de Graaf, M., Hakkarainen, J., Hassinen, S., Ialongo, I., Kleipool, Q., Krotkov, N., Li, C., Lamsal, L., Newman, P., Nowlan, C.,

Suleiman, R., Tilstra, L. G., Torres, O., Wang, H., and Wargan, K.: The Ozone Monitoring Instrument: Overview of 14 years in space, Atmos. Chem. Phys., 18, 5699-5745, doi:10.5194/acp-18-5699-2018, 2018.

745 Loyola, D. G., Garcia, S. G., Lutz, R., Argyrouli, A., Romahn, F., Spurr, R. J. D., Pedergnana, M., Doicu, A., Garcia, V. M., and Schussler, O.: The operational cloud retrieval algorithms from TROPOMI on board Sentinel-5 Precursor, Atmos. Meas. Tech., 11, 409-427, doi:10.5194/amt-11-409-2018, 2018a.

Loyola, D. G., Lutz, R., Argyrouli, A., and Spurr, R.: S5P/TROPOMI ATBD Cloud Products, https://sentinel.esa.int/documents/247904/2476257/Sentinel-5P-TROPOMI-ATBD-Clouds (Last accessed: 20 January 2020),
750 2018b.

Loyola, D. G., Thomas, W., Livschitz, Y., Ruppert, T., Albert, P., and Hollmann, R.: Cloud properties derived from GOME/ERS-2 backscatter data for trace gas retrieval, IEEE T. Geosci. Remote Sens., 45, 2747-2758, doi:10.1109/TGRS.2007.901043, 2007.

Marais, E. A., Jacob, D. J., Choi, S., Joiner, J., Belmonte-Rivas, M., Cohen, R. C., Beirle, S., Murray, L. T., Schiferl, L. D.,
755 Shah, V., and Jaegle, L.: Nitrogen oxides in the global upper troposphere: Interpreting cloud-sliced NO_2 observations from the OMI satellite instrument, Atmos. Chem. Phys., 18, 17017-17027, doi:10.5194/acp-18-17017-2018, 2018.

Mickley, L. J., Murti, P. P., Jacob, D. J., Logan, J. A., Koch, D. M., and Rind, D.: Radiative forcing from tropospheric ozone calculated with a unified chemistry-climate model, J. Geophys. Res.-Atmos., 104, 30153-30172, doi:10.1029/1999JD900439, 1999.

760 Murray, L. T., Jacob, D. J., Logan, J. A., Hudman, R. C., and Koshak, W. J.: Optimized regional and interannual variability of lightning in a global chemical transport model constrained by LIS/OTD satellite data, J. Geophys. Res.-Atmos., 117, D20307, doi:10.1029/2012jd017934, 2012.

Murray, L. T., Logan, J. A., and Jacob, D. J.: Interannual variability in tropical tropospheric ozone and OH: The role of lightning, J. Geophys. Res.-Atmos., 118, 11468-11480, doi:10.1002/jgrd.50857, 2013.

765 Nault, B. A., Garland, C., Wooldridge, P. J., Brune, W. H., Campuzano-Jost, P., Crounse, J. D., Day, D. A., Dibb, J., Hall, S. R., Huey, L. G., Jimenez, J. L., Liu, X. X., Mao, J. Q., Mikoviny, T., Peischl, J., Pollack, I. B., Ren, X. R., Ryerson, T. B., Scheuer, E., Ullmann, K., Wennberg, P. O., Wisthaler, A., Zhang, L., and Cohen, R. C.: Observational constraints on the oxidation of NO_x in the upper troposphere, J. Phys. Chem. A, 120, 1468-1478, doi:10.1021/acs.jpca.5b07824, 2016.

Newchurch, M. J., Allen, M., Gunson, M. R., Salawitch, R. J., Collins, G. B., Huston, K. H., Abbas, M. M., Abrams, M. C.,
770 Chang, A. Y., Fahey, D. W., Gao, R. S., Irion, F. W., Loewenstein, M., Manney, G. L., Michelsen, H. A., Podolske, J. R., Rinsland, C. P., and Zander, R.: Stratospheric NO and NO_2 abundances from ATMOS solar-occultation measurements, Geophys. Res. Lett., 23, 2373-2376, doi:10.1029/96GL01196, 1996.

Ott, L. E., Pickering, K. E., Stenchikov, G. L., Allen, D. J., DeCaria, A. J., Ridley, B., Lin, R. F., Lang, S., and Tao, W. K.: Production of lightning NO_x and its vertical distribution calculated from three-dimensional cloud-scale chemical transport
775 model simulations, J. Geophys. Res.-Atmos., 11510.1029/2009jd011880, 2010.

Pavelin, E. G., Johnson, C. E., Rughooputh, S., and Toumi, R.: Evaluation of pre-industrial surface ozone measurements made using Schönbein's method, Atmos. Environ., 33, 919-929, doi:10.1016/S1352-2310(98)00257-X, 1999.

Pinardi, G., Roozendael, M. V., Hendrick, F., Theys, N., Abuhassan, N., Bais, A., Boersma, K. F., Cede, A., Chong, J., Donner, S., Drosoglou, T., Frieß, U., Granville, J., Herman, J. R., Eskes, H., Holla, R., Hovila, J., Irie, H., Kanaya, Y., Karagkiozidis,
780   D., Kouremeti, N., Lambert, J.-C., Ma, J., Peters, E., Piters, A., Postylyakov, O., Richter, A., Remmers, J., Takashima, H., Tiefengraber, M., Valks, P., Vlemmix, T., Wagner, T., and Wittrock, F.: Validation of tropospheric NO_2 column measurements of GOME-2A and OMI using MAX-DOAS and direct sun network observations, Atmos. Chem. Phys. Discuss., 2020, 1-55, doi:10.5194/amt-2020-76, 2020.

Pour-Biazar, A., McNider, R. T., Roselle, S. J., Suggs, R., Jedlovec, G., Byun, D. W., Kim, S., Lin, C. J., Ho, T. C., Haines,
785   S., Dornblaser, B., and Cameron, R.: Correcting photolysis rates on the basis of satellite observed clouds, J. Geophys. Res.-Atmos., 112, 1-17, doi:10.1029/2006JD007422, 2007.

Price, C. and Rind, D.: A simple lightning parameterization for calculating global lightning distributions, J. Geophys. Res.-Atmos., 97, 9919-9933, doi:10.1029/92JD00719, 1992.

Puentedura, O., Gil, M., Saiz-Lopez, A., Hay, T., Navarro-Comas, M., Gómez-Pelaez, A., Cuevas, E., Iglesias, J., and Gomez,
790   L.: Iodine monoxide in the north subtropical free troposphere, Atmos. Chem. Phys., 12, 4909-4921, doi:10.5194/acp-12-4909-2012, 2012.

Reed, C., Evans, M. J., Di Carlo, P., Lee, J. D., and Carpenter, L. J.: Interferences in photolytic NO_2 measurements: explanation for an apparent missing oxidant?, Atmos. Chem. Phys., 16, 4707-4724, doi:10.5194/acp-16-4707-2016, 2016.

Ridley, B., Ott, L., Pickering, K., Emmons, L., Montzka, D., Weinheimer, A., Knapp, D., Grahek, F., Li, L., Heymsfield, G.,
795   McGill, M., Kucera, P., Mahoney, M. J., Baumgardner, D., Schultz, M., and Brasseur, G.: Florida thunderstorms: A faucet of reactive nitrogen to the upper troposphere, J. Geophys. Res.-Atmos., 109, 1-19, doi:10.1029/2004JD004769, 2004.

Rivera, C., Stremme, W., and Grutter, M.: Nitrogen dioxide DOAS measurements from ground and space: Comparison of zenith scattered sunlight ground-based measurements and OMI data in Central Mexico, Atmósfera, 26, 401-414, doi:10.1016/S0187-6236(13)71085-3, 2013.

800   Robles-Gonzalez, C., Navarro-Comas, M., Puentedura, O., Schneider, M., Hase, F., Garcia, O., Blumenstock, T., and Gil-Ojeda, M.: Intercomparison of stratospheric nitrogen dioxide columns retrieved from ground-based DOAS and FTIR and satellite DOAS instruments over the subtropical Izaña station, Atmos. Meas. Tech., 9, 4471-4485, doi:10.5194/amt-9-4471-2016, 2016.

Schenkeveld, V. M. E., Jaross, G., Marchenko, S., Haffner, D., Kleipool, Q. L., Rozemeijer, N. C., Veefkind, J. P., and Levelt,
805   P. F.: In-flight performance of the Ozone Monitoring Instrument, Atmos. Meas. Tech., 10, 1957-1986, doi:10.5194/amt-10-1957-2017, 2017.

Schreier, S. F., Richter, A., Wittrock, F., and Burrows, J. P.: Estimates of free-tropospheric NO_2 and HCHO mixing ratios derived from high-altitude mountain MAX-DOAS observations at midlatitudes and in the tropics, Atmos. Chem. Phys., 16, 2803-2817, doi:10.5194/acp-16-2803-2016, 2016.

Schumann, U.: The impact of nitrogen oxides emissions from aircraft upon the atmosphere at flight altitudes—results from the AERONOX project, Atmos. Environ., 31, 1723-1733, doi:10.1016/S1352-2310(96)00326-3, 1997.

Schumann, U. and Huntrieser, H.: The global lightning-induced nitrogen oxides source, Atmos. Chem. Phys., 7, 3823-3907, doi:10.5194/acp-7-3823-2007, 2007.

Silvern, R. F., Jacob, D. J., Mickley, L. J., Sulprizio, M. P., Travis, K. R., Marais, E. A., Cohen, R. C., Laughner, J. L., Choi, S., Joiner, J., and Lamsal, L. N.: Using satellite observations of tropospheric NO_2 columns to infer long-term trends in US NO_x emissions: The importance of accounting for the free tropospheric NO_2 background, Atmos. Chem. Phys., 19, 8863-8878, doi:10.5194/acp-19-8863-2019, 2019.

Silvern, R. F., Jacob, D. J., Travis, K. R., Sherwen, T., Evans, M. J., Cohen, R. C., Laughner, J. L., Hall, S. R., Ullmann, K., Crounse, J. D., Wennberg, P. O., Peischl, J., and Pollack, I. B.: Observed NO/NO_2 ratios in the upper troposphere imply errors in $NO-NO_2-O_3$ cycling kinetics or an unaccounted NO_x reservoir, Geophys. Res. Lett., 45, 4466–4474, doi:10.1029/2018GL077728, 2018.

Sioris, C. E., Kurosu, T. P., Martin, R. V., and Chance, K.: Stratospheric and tropospheric NO_2 observed by SCIAMACHY: First results, Adv. Spac Res., 34, 780-785, doi:10.1016/j.asr.2003.08.066, 2004.

Stammes, P., Sneep, M., de Haan, J. F., Veefkind, J. P., Wang, P., and Levelt, P. F.: Effective cloud fractions from the Ozone Monitoring Instrument: Theoretical framework and validation, J. Geophys. Res.-Atmos., 113, 1-12, doi:10.1029/2007JD008820, 2008.

Stavrakou, T., Muller, J. F., Boersma, K. F., van der A, R. J., Kurokawa, J., Ohara, T., and Zhang, Q.: Key chemical NO_x sink uncertainties and how they influence top-down emissions of nitrogen oxides, Atmos. Chem. Phys., 13, 9057-9082, doi:10.5194/acp-13-9057-2013, 2013.

Stettler, M. E. J., Eastham, S., and Barrett, S. R. H.: Air quality and public health impacts of UK airports. Part I: Emissions, Atmos. Environ., 45, 5415-5424, doi:10.1016/j.atmosenv.2011.07.012, 2011.

Stratmann, G., Ziereis, H., Stock, P., Brenninkmeijer, C. A. M., Zahn, A., Rauthe-Schoch, A., Velthoven, P. V., Schlager, H., and Volz-Thomas, A.: NO and NO_y in the upper troposphere: Nine years of CARIBIC measurements onboard a passenger aircraft, Atmos. Environ., 133, 93-111, doi:10.1016/j.atmosenv.2016.02.035, 2016.

Thomas, K., Berg, M., Boulanger, D., Houben, N., Gressent, A., Nedelec, P., Patz, H. W., Thouret, V., and Volz-Thomas, A.: Climatology of NO_y in the troposphere and UT/LS from measurements made in MOZAIC, Tellus B, 67, 1-16, doi:10.3402/tellusb.v67.28793, 2015.

Toledano, C., Gonzalez, R., Fuertes, D., Cuevas, E., Eck, T. F., Kazadzis, S., Kouremeti, N., Grobner, J., Goloub, P., Blarel, L., Roman, R., Barreto, A., Berjon, A., Holben, B. N., and Cachorro, V. E.: Assessment of Sun photometer Langley calibration at the high-elevation sites Mauna Loa and Izaña, Atmos. Chem. Phys., 18, 14555-14567, doi:10.5194/acp-18-14555-2018, 2018.

Torres, O., Bhartia, P. K., Jethva, H., and Ahn, C.: Impact of the ozone monitoring instrument row anomaly on the long-term record of aerosol products, Atmos. Meas. Tech., 11, 2701-2715, doi:10.5194/amt-11-2701-2018, 2018.

Tost, H., Jockel, P. J., and Lelieveld, J.: Lightning and convection parameterisations - uncertainties in global modelling, Atmos.
845 Chem. Phys., 7, 4553-4568, doi:10.5194/acp-7-4553-2007, 2007.

Travis, K. R., Jacob, D. J., Fisher, J. A., Kim, P. S., Marais, E. A., Zhu, L., Yu, K., Miller, C. C., Yantosca, R. M., Sulprizio, M. P., Thompson, A. M., Wennberg, P. O., Crounse, J. D., St Clair, J. M., Cohen, R. C., Laughner, J. L., Dibb, J. E., Hall, S. R., Ullmann, K., Wolfe, G. M., Pollack, I. B., Peischl, J., Neuman, J. A., and Zhou, X. L.: Why do models overestimate surface ozone in the Southeast United States?, Atmos. Chem. Phys., 16, 13561-13577, doi:10.5194/acp-16-13561-2016, 2016.

850 van der A, R. J., de Laat, A. T. J., Ding, J., and Eskes, H. J.: Connecting the dots: NO_x emissions along a West Siberian natural gas pipeline, NPJ Clim. Atmos. Sci., 3, 16, doi:10.1038/s41612-020-0119-z, 2020.

van Geffen, J., Boersma, K. F., Eskes, H., Sneep, M., ter Linden, M., Zara, M., and Veefkind, J. P.: S5P TROPOMI NO_2 slant column retrieval: Method, stability, uncertainties and comparisons with OMI, Atmos. Meas. Tech., 13, 1315-1335, doi:10.5194/amt-13-1315-2020, 2020.

855 van Geffen, J., Eskes, H. J., Boersma, K. F., Maasakkers, J. D., and Veefkind, J. P.: TROPOMI ATBD of the total and tropospheric NO_2 data products, https://sentinel.esa.int/documents/247904/2476257/Sentinel-5P-TROPOMI-ATBD-NO2-data-products (Last accessed: 20 January 2020), 2019.

Veefkind, J. P., de Haan, J. F., Sneep, M., and Levelt, P. F.: Improvements to the OMI O2–O2 operational cloud algorithm and comparisons with ground-based radar–lidar observations, Atmos. Meas. Tech., 9, 6035-6049, doi:10.5194/amt-9-6035-860 2016, 2016.

Verhoelst, T., Compernolle, S., Pinardi, G., Lambert, J. C., Eskes, H. J., Eichmann, K. U., Fjæraa, A. M., Granville, J., Niemeijer, S., Cede, A., Tiefengraber, M., Hendrick, F., Pazmiño, A., Bais, A., Bazureau, A., Boersma, K. F., Bognar, K., Dehn, A., Donner, S., Elokhov, A., Gebetsberger, M., Goutail, F., Grutter de la Mora, M., Gruzdev, A., Gratsea, M., Hansen, G. H., Irie, H., Jepsen, N., Kanaya, Y., Karagkiozidis, D., Kivi, R., Kreher, K., Levelt, P. F., Liu, C., Müller, M., Navarro 865 Comas, M., Piters, A. J. M., Pommereau, J. P., Portafaix, T., Puentedura, O., Querel, R., Remmers, J., Richter, A., Rimmer, J., Rivera Cárdenas, C., Saavedra de Miguel, L., Sinyakov, V. P., Strong, K., Van Roozendael, M., Veefkind, J. P., Wagner, T., Wittrock, F., Yela González, M., and Zehner, C.: Ground-based validation of the Copernicus Sentinel-5p TROPOMI NO_2 measurements with the NDACC ZSL-DOAS, MAX-DOAS and Pandonia global networks, Atmos. Meas. Tech. Discuss., 2020, 1-40, doi:10.5194/amt-2020-119, 2020.

870 Verlinden, K. L., Thompson, D. W. J., and Stephens, G. L.: The three-dimensional distribution of clouds over the southern hemisphere high latitudes, J. Climate, 24, 5799-5811, doi:10.1175/2011JCLI3922.1, 2011.

Wang, P., Piters, A., van Geffen, J., Tuinder, O., Stammes, P., and Kinne, S.: Shipborne MAX-DOAS measurements for validation of TROPOMI NO_2 products, Atmos. Meas. Tech., 13, 1413-1426, doi:10.5194/amt-13-1413-2020, 2020a.

Wang, P., Stammes, P., van der A, R., Pinardi, G., and van Roozendael, M.: FRESCO+: An improved O2 A-band cloud 875 retrieval algorithm for tropospheric trace gas retrievals, Atmos. Chem. Phys., 8, 6565-6576, doi:10.5194/acp-8-6565-2008, 2008.

Wang, Z., Zhang, X., Liu, L., Cheng, M., and Xu, J.: Spatial and seasonal patterns of atmospheric nitrogen deposition in North China, Atmos. Ocean. Sci. Lett., 13, 188-194, doi:10.1080/16742834.2019.1701385, 2020b.

Wendisch, M., Pöschl, U., Andreae, M. O., Machado, L. A. T., Albrecht, R., Schlager, H., Rosenfeld, D., Martin, S. T.,
880   Abdelmonem, A., Afchine, A., Araùjo, A. C., Artaxo, P., Aufmhoff, H., Barbosa, H. M. J., Borrmann, S., Braga, R., Buchholz, B., Cecchini, M. A., Costa, A., Curtius, J., Dollner, M., Dorf, M., Dreiling, V., Ebert, V., Ehrlich, A., Ewald, F., Fisch, G., Fix, A., Frank, F., Fütterer, D., Heckl, C., Heidelberg, F., Hüneke, T., Jäkel, E., Järvinen, E., Jurkat, T., Kanter, S., Kästner, U., Kenntner, M., Kesselmeier, J., Klimach, T., Knecht, M., Kohl, R., Kölling, T., Krämer, M., Krüger, M., Krisna, T. C., Lavric, J. V., Longo, K., Mahnke, C., Manzi, A. O., Mayer, B., Mertes, S., Minikin, A., Molleker, S., Münch, S., Nillius, B.,
885   Pfeilsticker, K., Pöhlker, C., Roiger, A., Rose, D., Rosenow, D., Sauer, D., Schnaiter, M., Schneider, J., Schulz, C., de Souza, R. A. F., Spanu, A., Stock, P., Vila, D., Voigt, C., Walser, A., Walter, D., Weigel, R., Weinzierl, B., Werner, F., Yamasoe, M. A., Ziereis, H., Zinner, T., and Zöger, M.: ACRIDICON–CHUVA campaign: Studying tropical deep convective clouds and precipitation over Amazonia using the new German research aircraft HALO, BAMS, 97, 1885-1908, doi:10.1175/BAMS-D-14-00255.1, 2016.

890   Williams, J. E., Boersma, K. F., Le Sager, P., and Verstraeten, W. W.: The high-resolution version of TM5-MP for optimized satellite retrievals: description and validation, Geosci. Model Dev., 10, 721-750, doi:10.5194/gmd-10-721-2017, 2017.

Worden, H. M., Bowman, K. W., Kulawik, S. S., and Aghedo, A. M.: Sensitivity of outgoing longwave radiative flux to the global vertical distribution of ozone characterized by instantaneous radiative kernels from Aura-TES, J. Geophys. Res.-Atmos., 116, 1-15, doi:10.1029/2010jd015101, 2011.

895   Zhao, B., Wang, S. X., Liu, H., Xu, J. Y., Fu, K., Klimont, Z., Hao, J. M., He, K. B., Cofala, J., and Amann, M.: NO_x emissions in China: historical trends and future perspectives, Atmos. Chem. Phys., 13, 9869-9897, doi:10.5194/acp-13-9869-2013, 2013.

Zhao, X., Griffin, D., Fioletov, V., McLinden, C., Cede, A., Tiefengraber, M., Müller, M., Bognar, K., Strong, K., Boersma, F., Eskes, H., Davies, J., Ogyu, A., and Lee, S. C.: Assessment of the quality of TROPOMI high-spatial-resolution NO_2 data products in the Greater Toronto Area, Atmos. Meas. Tech., 13, 2131-2159, doi:10.5194/amt-13-2131-2020, 2020.

900   Ziemke, J. R., Chandra, S., and Bhartia, P. K.: "Cloud slicing": A new technique to derive upper tropospheric ozone from satellite measurements, J. Geophys. Res.-Atmos., 106, 9853-9867, doi:10.1029/2000jd900768, 2001.